# Hydrothermal growth of zinc oxide nanorods doped with manganese

Rajni Bagga

A Thesis
In
The Department
of
Physics

Presented in Partial Fulfillment of the Requirements
for the Degree of Master of Science (Physics) at
Concordia University
Montreal, Quebec, Canada

March 2020

**CONCORDIA UNIVERSITY**

**School of Graduate Studies**

This is to certify that the thesis prepared

By: **Rajni Bagga**

Entitled: **Hydrothermal growth of zinc oxide nanorods doped with manganese**

and submitted in partial fulfillment of the requirements for the degree of

**Master of Physics**

complies with the regulations of this University and meets the accepted standards with respect to originality and quality.

Signed by the final examining committee:

_____Chair

Dr. Brandon Helfield

_____Examiner

Dr. Laszlo Kalman

_____Examiner

Dr. Calvin Kalman

_____Supervisor

Dr. Pablo Bianucci

_____Co-Supervisor

Dr. Truong Vo-Van

Approved _____

Dr. Alexandre Champagne, Chair of Department

Dr. Valter Zazubovits Graduate Program Director

2020 _____

Dr. André Roy, Dean Faculty of Arts and Science

# ABSTRACT


## Hydrothermal growth of zinc oxide nanorods doped with manganese

Rajni Bagga

ZnO nanostructures can be grown using a variety of techniques. Using a hydrothermal method, ZnO nanostructures can be produced easily on a large scale due to the low temperature involved. ZnO is a well-studied wide-band gap (3.37 eV) n-type semiconductor material with significant properties such as a large exciton binding energy (60 meV). In this project we have chosen the hydrothermal method to synthesize undoped and manganese doped zinc oxide nanorods at different growth temperatures of $60^0$C, $70^0$C, $80^0$C, and $90^0$C respectively for 20h. We made a seed layer of ZnO on the Si substrate by annealing zinc acetate at $400^0$ C. The morphology of the nanorods was visualised by taking their side and top SEM images. Micro Raman Spectra shows the crystal orientation of the nanorods with respect to substrate and optical Raman-active modes of undoped and doped nanorods. Room-temperature micro-Photoluminescence spectra of nanorods shows the sharp near band emission at 383 nm and broadband defect emission in the visible range. From EPR spectroscopy we find out whether a significant amount of Mn was incorporated into nanorods. Our findings indicate that the presence of Mn in the growth medium results in improved morphology, even though at the lowest growth temperatures there is no clear incorporation of Mn into the nanorods. This implies that the presence of the Mn ions in the group medium is enough to increase the growth rates of ZnO, regardless of whether the ions are incorporated into the crystal or not.

# Acknowledgement

I am deeply thankful to my main supervisor Dr. Pablo Bianucci for his excellent guidance, intellectual support and continuous support for my M.Sc. study. He is a very talented and passionate scientist. It is not easy to find a supervisor like Dr. Pablo Bianucci. Thank you so much for leaving your doors open when I needed your help. You always there to help me when I got stuck with problem in my research work.

I would also like to thank my co-supervisor Dr. Truong Vo-Van who had supported me in my difficult time with financial support, his insight comments and encouragement throughout this study.

This thesis got finished with the help of lab technicians Zelko and Patrick who have helped a lot. I really appreciate Dr. Amir Hassanpour for giving me proper guidance in preparation of nanorods.

Many thanks to Marie-Anne Cheong Youne for her kindness and her assistance with departmental matters.

I owe my gratitude towards my lab-mates and dearest friends Kathleen, Samar, Math, Alexis, Alax, Eric, Denial Moddaferi, Shubam for their infinite support patience and kindness. I feel very lucky to meet such great people. I can not forget the time which we have spent together.

My special thanks to my husband and my best friend Sahil. He encouraged me with his endless love. His suggestions are always valuable for me. His priceless support has been very important for me. He is the reason I have been able to push myself to achieve all that I have.

I am thankful to my parents and my loving sister and brothers for supporting me all times. My elder brother always gave me guidelines for choosing right path for me. He always motivate me when I have any kind of difficulties.

I am grateful to Concordia University for financial support and for giving me chance to be a graduate research student.

# Contents

# List of Figures

**List of tables**

# Abbreviations

1D 1-dimensional

Mn Manganese

SEM Scanning electron microscopy

PL Photoluminescence

TO Transverse optical

LO Longitudinal optical

NBE Near Band Edge

UV Ultraviolet

RS Raman Spectroscopy

ESR Electron Spin Resonance

CVD Chemical vapour deposition

PLD Pulsed laser deposition

MBE Molecular beam epitaxy

NRs Nanorod

# Chapter 1

# Introduction

## 1.1 Introduction

ZnO is an interesting material because of its significant and unique properties, such as a direct energy gap (3.37 eV) with large exciton binding energy (~ 60 meV) which means that its excitons are stable at room temperature as compared to other semiconductors [1]. In addition, it is inexpensive, non-toxic, and nature-abundant. It is also considered as biocompatible [38].

Thanks to these properties, ZnO has gained considerable attention from researchers over the past few years. By synthesising ZnO rods in nanoscale form, the optical, electrical and magnetic properties of ZnO can be improved [2]. ZnO is widely used in the production of electronic devices. Since it is easy to produce nanorods/nanowires and electromechanical coupling in ZnO [62], it is used to produce gas sensors [3] and solar cells [4]. Due to their low cost, ease of synthesis, and high stability, ZnO nanorods are widely used in solar cells [4], light emitting diodes [5] and photodetectors [6].

The applications of ZnO nanorods are not only limited to electronic devices or engineering fields, they are also useful in cosmetics, the pharmaceutical industry, and the food packaging industry [63].

### 1.2 Contributions

In this thesis, we have prepared undoped and Mn-doped ZnO nanorods on silicon substrates by using a hydrothermal method. The hydrothermal method is inexpensive for the growth of nanorods. We made a seeding layer of ZnO nanoparticles on the cleaned Silicon substrate by annealing zinc acetate at $400^0$C for 30 minutes. To grow the nanorods, the substrate was placed in the growth vessel containing solution of zinc nitrate and HMTA dissolved in deionised water.

What differentiates this work from previous ones is that we have done a systematic study of the growth temperature using the values of $60^0$C, $70^0$C, $80^0$C and $90^0$C, both for undoped and Mn-doped ZnO nanorods [18].

For the characterisation of nanorods we used different techniques. For a morphology inspection SEM is used, and we see that diameter and length of the nanorods increase with higher growth temperature. PL, Raman spectroscopy, EPR support a trend where the number of defects in the material becomes larger from $60^0$C and $70^0$C, and then decreases when the growth temperature increases at $80^0$C and $90^0$C. From EPR spectroscopy we find out that significant amounts of Mn were incorporated into nanorods only at $80^0$C and $90^0$C.

## 1.3 Thesis Outline

This thesis contains 6 chapters. Chapter 1 provides general information, contributions and the thesis outline.

In chapter 2, we briefly review the theoretical background of ZnO nanorods and the techniques which are used for their characterisation.

In chapter 3, we explain the systematic characterisation of undoped ZnO nanorods by using SEM, Raman Spectroscopy, Photoluminescence and ESR spectroscopy.

In chapter 4, the characterisation of Mn-doped ZnO nanorods by using SEM, Raman Spectroscopy, Photoluminescence and ESR spectroscopy was discussed.

In chapter 5, we compare the results of undoped and Mn-doped ZnO nanorods. In chapter 6 we present the main conclusions of the thesis work.

# Chapter 2

## 2.1 Introduction

In this chapter, we discuss the general properties of ZnO, preparation methods, experimental techniques for characterisation, and some of its applications. We introduce several growth techniques and discuss hydrothermal growth of nanorods in detail. We introduce all the techniques that we used to do the characterisation of our samples. Finally, we discuss the theoretical background and review the literature on the properties and applications of ZnO.

## 2.2 Properties of ZnO

ZnO is a II-VI group compound semiconductor. It has hexagonal wurtzite type structure [7]. Other favourable properties of ZnO are that is a non-toxic, cheap, relatively abundant material, and it is chemically stable. At low growth temperatures, it has many native defects such as oxygen vacancies ($V_o$), interstitial zinc atoms ($Zn_i$), Zinc vacancies ($V_{Zn}$), interstitial oxygen atoms ($O_i$) and background impurities such as hydrogen [64]. Some of defects are sources of deep level light emissions and some are shallow which lead to n-doping of as-grown materials [65].

### 2.2.1 Crystal structure properties of ZnO

At normal atmospheric pressure, ZnO is in the hexagonal wurtzite crystal structure as it is the most stable one [8]. Figure 1 shows a crystal structure model of hexagonal wurtzite ZnO. The wurtzite crystal structure of ZnO consists of alternating zinc (Zn) and oxygen (O) atoms. Each oxygen ion ($O^{2-}$) is surrounded tetrahedrally by four zinc ions ($Zn^{2+}$). ZnO has two polar surfaces the Zn (0001) and O (0001) terminated faces, and two non-polar surfaces (1120) and (1010) which possess an equal number of Zn and O atoms. The polar surfaces have a normal dipole moment along c-axis due to oppositely charged ions for $Zn^{-}$ and $O^{-}$ which leads to the production of positively charged (0001) and negatively charged ($000\bar{1}$) surfaces. The structure of ZnO is stable because the $\pm$(0001) surfaces of ZnO are automatically stable and flat [8].

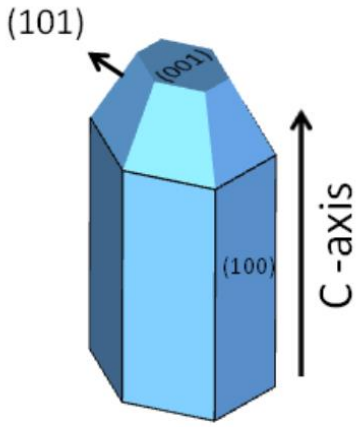


Figure 1: Crystal structure model of hexagonal wurtzite ZnO

# 2.3 Growth methods of ZnO nanorods

There are several growth methods that have been recently developed to grow ZnO nanorods including chemical vapour deposition (CVD) [24-26], hydrothermal growth, molecular beam

epitaxy (MBE) [27], pulsed laser deposition (PLD) [28], sputtering [29] electrospinning [66], and so on. We chose the most common hydrothermal method to grow the nanorods. The hydrothermal method has many advantages over the synthesis techniques which have been discussed many times in the literature [9].

### 2.3.1 Hydrothermal method

For all samples we cleaned the substrate with three 10-minute steps in an ultrasonic bath with acetone, isopropanol alcohol and deionised water. We prepared a 5 mM precursor solution of Zinc acetate in pure ethanol as seed solution. The seed solution was drop casted on the substrate for 7 times, and the substrate annealed at $400^0$ C for 30 minutes so that zinc acetate decomposed into ZnO nanoparticles. This process was completed two times for each sample to get the proper seed coverage.

We have used a silicon substrate because it is less expensive, and it has high conductivity for SEM images. In the most common hydrothermal method, salt of zinc nitrate hexahydrate and Hexamethylene tetraamine (HMTA) were dissolved into the nutrient medium such as water with the same ratio. Both solutions had a 50 mM concentration. For the growth of nanorods, the substrate was placed into a growth solution in a hermetic bottle. To dope the nanorods with manganese, we added 1% manganese acetate tetrahydrate into the growth vessel as the molarity of zinc and HMTA dissolved into deionised water was kept constant at 50 mM [53].

Once the growth time was over, we took the sample of the bottle, washed the sample with deionised water and dried it using dry nitrogen.

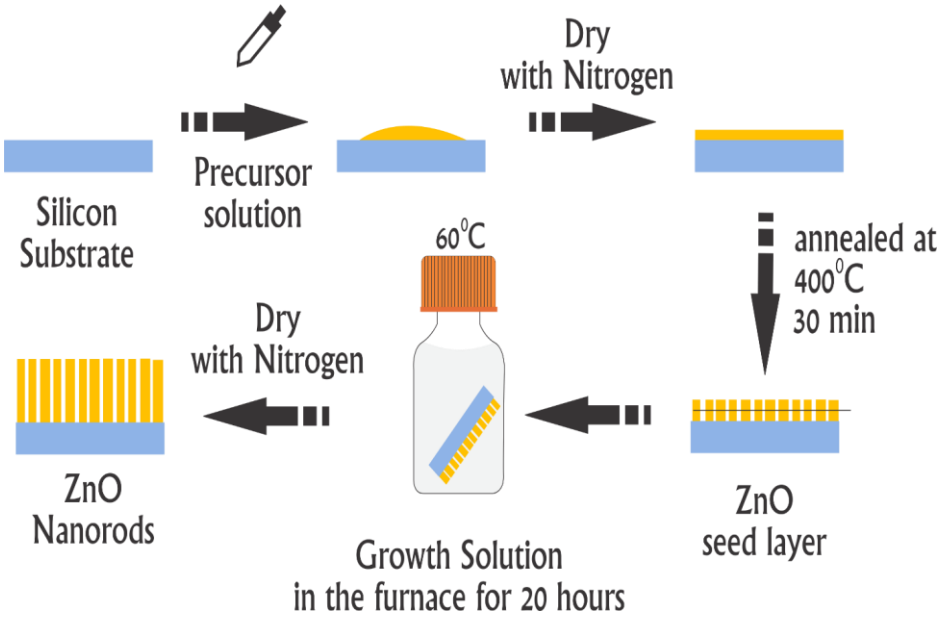


Figure 2: Schematic view of growth process

We have used four different temperatures for the growth of ZnO and Mn-doped ZnO nanorods which are 60ᵘ C, 70ᵘ C, 80ᵘ C, and 90ᵘ C.

# 2.4 Experimental techniques for characterisation

## 2.4.1 Scanning Electron Microscopy

The scanning electron microscope (SEM) is a type of electron microscope capable of producing high resolution images of the sample surface [11]. The SEM technique can characterise the two-

dimensional appearance and is useful to get information about the surface structure of the sample. In a scanning electron microscope there is a gun inside, which generates a beam of electrons in the vacuum created inside the chamber where we put the samples for analysis. That beam is collimated by the electromagnetic condenser lenses, focused by an objective lens, and scanned across the surface of the sample by electromagnetic deflection coils. The primary imaging method is by collecting the secondary electrons which are released by the sample. By corelating the sample scan position with the resulting signal, a black and white image is formed which is like what would be seen through an optical microscope that have similar magnification [11]. The short wavelength of the electrons allows for imaging at much higher spatial resolution than is achievable with optical microscopes.

By using SEM technique, we get the information about the nanorods like the orientation, length, diameter and shape.

### 2.4.2 Raman spectroscopy

Raman spectroscopy is a technique typically used to determine vibrational modes of molecules [67]. Raman spectroscopy is a non-invasive way of probing the crystal structure, phonon frequencies, composition and presence of free carriers and defects in a semi-conductor. When monochromatic radiation of definite frequency is passed through a substance, light is scattered. The transmitted light with same frequency as that of incident radiation is called Rayleigh scattering. A small amount of scattered light has a different frequency and is called Raman Scattering. In crystals, Raman scattering gives information about phonon modes, and the crystal structure of the sample. The laser power which is used in Raman spectroscopy is too low to damage

the sample under observation. On the straightforward Raman spectroscopy there are many variations. When the incident probing light has energy larger than the band gap then the resonance Raman occurs and increases the sensitivity of certain modes [12].

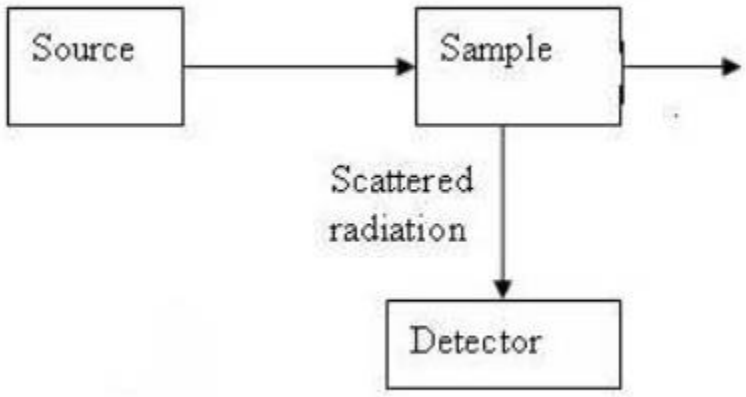


Figure 3: Block diagram of Raman Spectroscopy(https://www.sas.upenn.edu/~crulli/TheRamanSpectrophotometer.html)

## 2.4.3 Photoluminescence Spectroscopy

Photoluminescence spectroscopy is a non-destructive and contactless technique to probe the electronic structures of the materials. Light is shined on the samples and then samples absorbs that light. Then, upon deexcitation, light is emitted by the sample and this mechanism is called photoluminescence. In order to probe the band gap of the material, light having shorter wavelength is useful to excite the material. Photoexcitation causes the electrons within the material is valence band to move into permissible excited states. The excess energy is released when these electrons return to their equilibrium states. The excess energy may be released with emission of light (radiative process) or without it (non-radiative process). When the light is emitted, its energy light relates to the difference in energy levels between the two electron states involved in the transition

(the excited and equilibrium states). The intensity and spectral content of this photoluminescence is a measurement of many properties of material such as composition, structure, impurities, kinetic processes and energy transfer [30].

PL spectroscopy was performed with an excitation wavelength of 369 nm in air for our sample. The excitation laser was incident on the sample at a glancing angle. The emission from the sample was collected with a NUV-optimized microscope objective and dispersed by a grating spectrometer and then imaged by a CCD detector [31].

The experimental setup for photoluminescence is shown in figure 4.

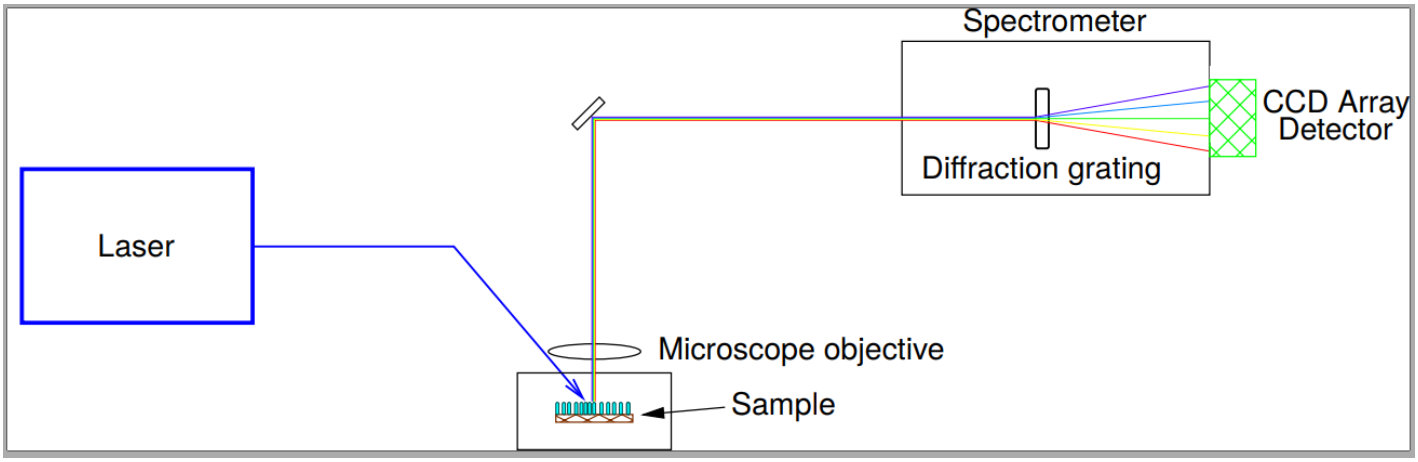


Figure 4: Block diagram of Photoluminescence spectroscopy

## 2.4.4 ESR Spectroscopy

ESR spectroscopy is a technique which can directly identify unpaired electrons. The materials which contains the unpaired electrons are called paramagnetic materials. They exhibit a net

magnetic moment in an external magnetic field. That's why this technique is also called electron paramagnetic resonance (EPR) spectroscopy [32, 33].

ESR spectroscopy can detect all kinds of paramagnetic species like free radicals in solids, liquids and aqueous solutions, transition metal ions, systems having more than one unpaired electrons, point defects in crystals, and systems with conducting electrons (metals and semiconductors).

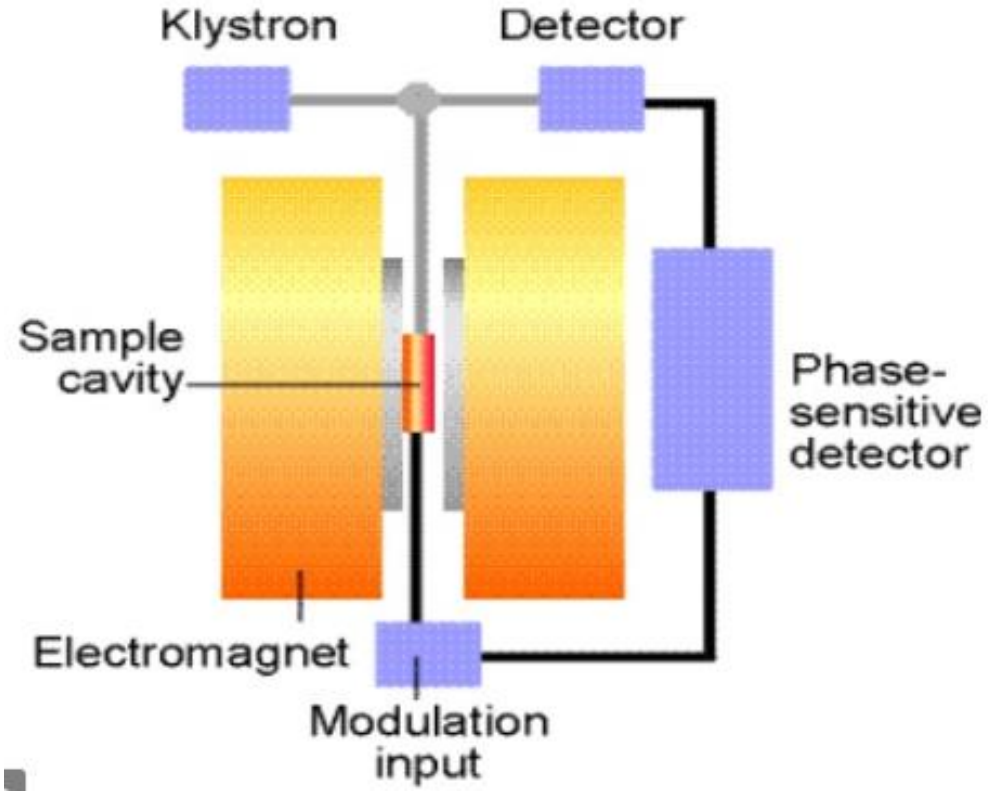


Figure 5: Block diagram of ESR Spectrometer

(https://www.globalspec.com/learnmore/labware_scientific_instruments/spectrometers_analytical_photometers/esrepr_spectrometers

In various fields of study such as chemistry, biology, and physics EPR has become a powerful analytical technique to detect and identify paramagnetic centers and free radicals [34, 35].

# Chapter 3

# Systematic study of ZnO nanorods grown at different temperatures

## 3.1. Introduction

In this chapter, we are going to discuss the results from our growth of undoped ZnO nanorods. We have samples grown at different temperatures $60^0$C, $70^0$C, $80^0$C, $90^0$C. We have used the different techniques, described in Chapter 2 to characterize the ZnO nanorods like SEM, Raman Spectroscopy, Photoluminescence spectroscopy, and EPR spectroscopy.

## 3.2. Morphology

SEM images of undoped ZnO nanorods grown at $60^0$C are shown in figure 6.

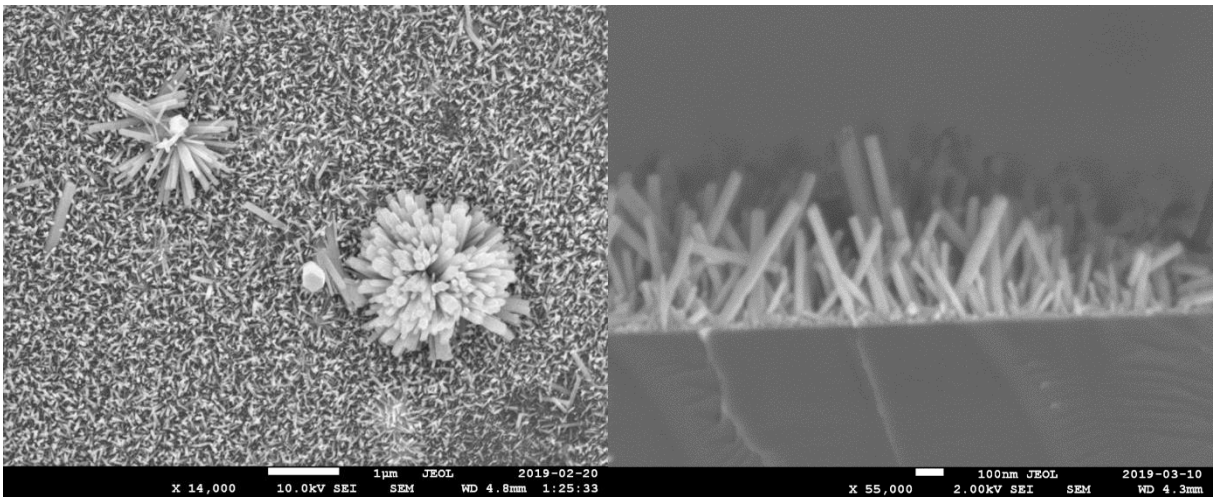


Figure 6: SEM images of undoped ZnO nanorods grown at $60^0$C. Left is image of top view and right is image of side view.

The rod shape is hexagonal. The nanorods average length is 372 nm and their average diameter is 68 nm. We saw some flower-like structures of nanorods which are due to nucleation sites [36]. These likely are heterogeneous nucleation sites since the interfacial energy between nanorods and substrate is smaller than the interfacial energy between nanorods and solution.

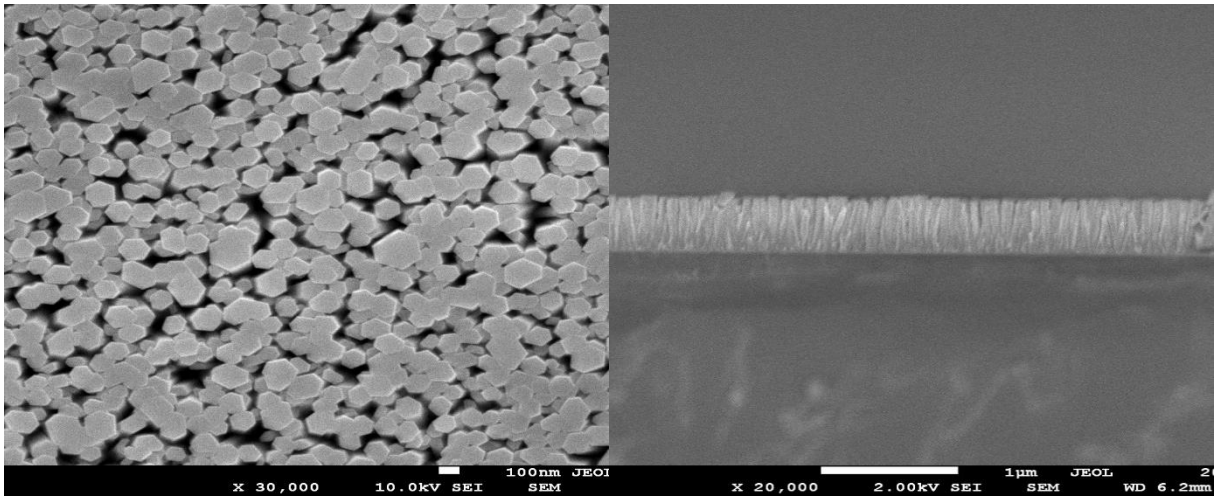


Figure 7: SEM images of undoped ZnO nanorods grown at $70^0$C. Left is the image of a top view and right is the image of a side view

ZnO nanorods grown at $70^0$C are shown in figure 7. We can see that the average length of nanorods is increased as compared to the average length at $60^0$C, also the average diameter increases. The orientation of nanorods improves at $70^0$C and they are more uniform. Most of the nanorods are oriented perpendicular to the substrate. The average length is 529 nm and their average diameter is 122 nm.

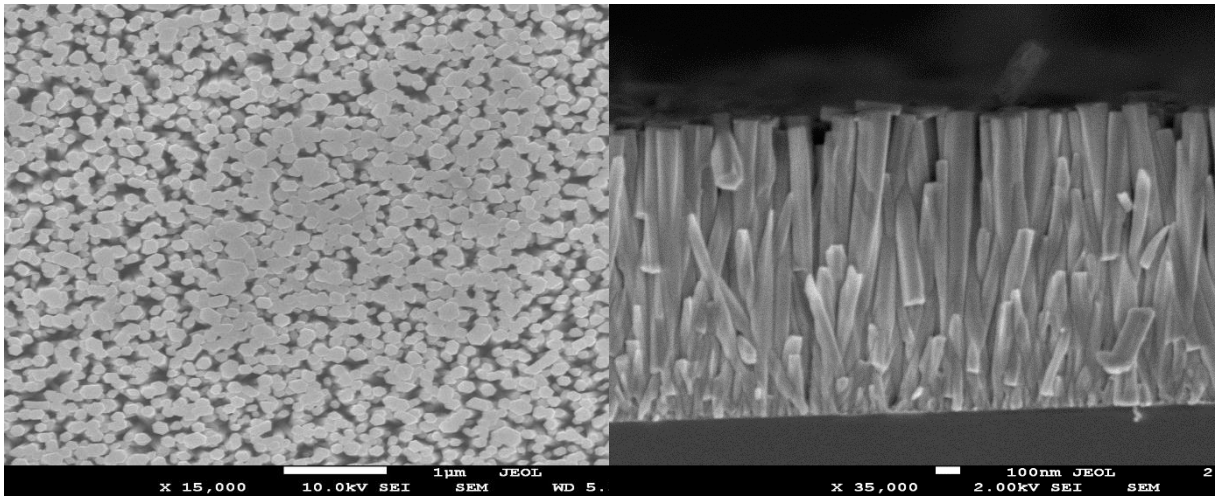


Figure 8: SEM images of undoped ZnO nanorods grown at $80^0$C. Left is the image of a top view and right is the image of a side view.

We can see from figure 8 that nanorods grown at $80^0$C are denser as compared to $60^0$C and $70^0$C. By comparing with the growth temperatures $60^0$C and $70^0$C, the average length and diameter at $80^0$C of nanorods increases. At a growth temperature of $80^0$C, the length is 1577 nm and the diameter is 135 nm respectively.

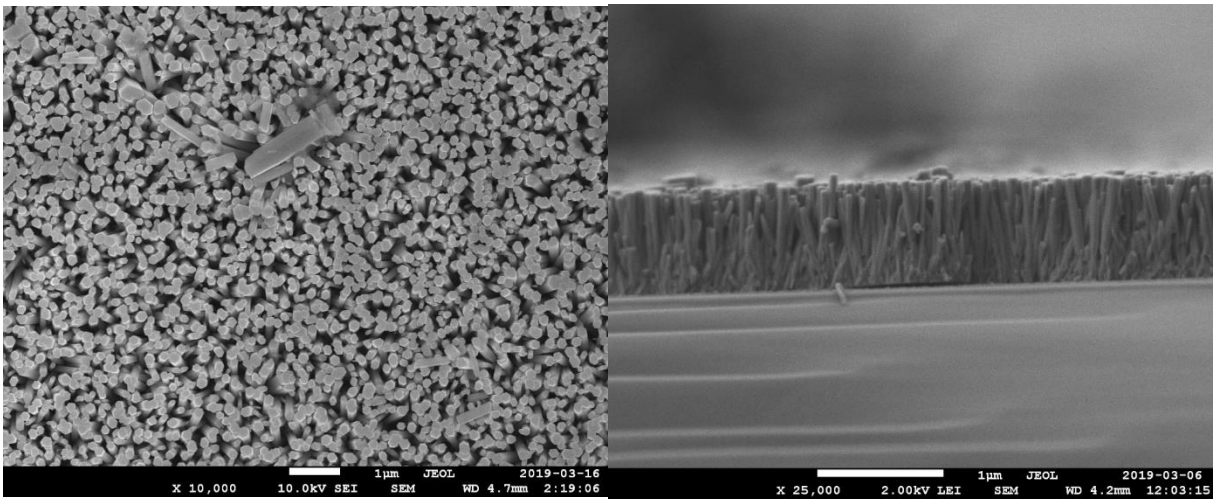


Figure 9: SEM images of undoped ZnO nanorods grown at $90^0$C. Left is the image of a top view and right is the image of a side view.

At $90^0$C, the average diameter and average length of the nanorods further increased. The orientation of the nanorods becomes significantly better at higher temperatures. The average length is 1620 nm and their average diameter is 158 nm.

In Figure 10, we put all the SEM images together with the top view and side view of the nanorods to make it easier to compare the different morphologies. It can be seen how the density and orientation becomes improved with the variations of growth temperatures.

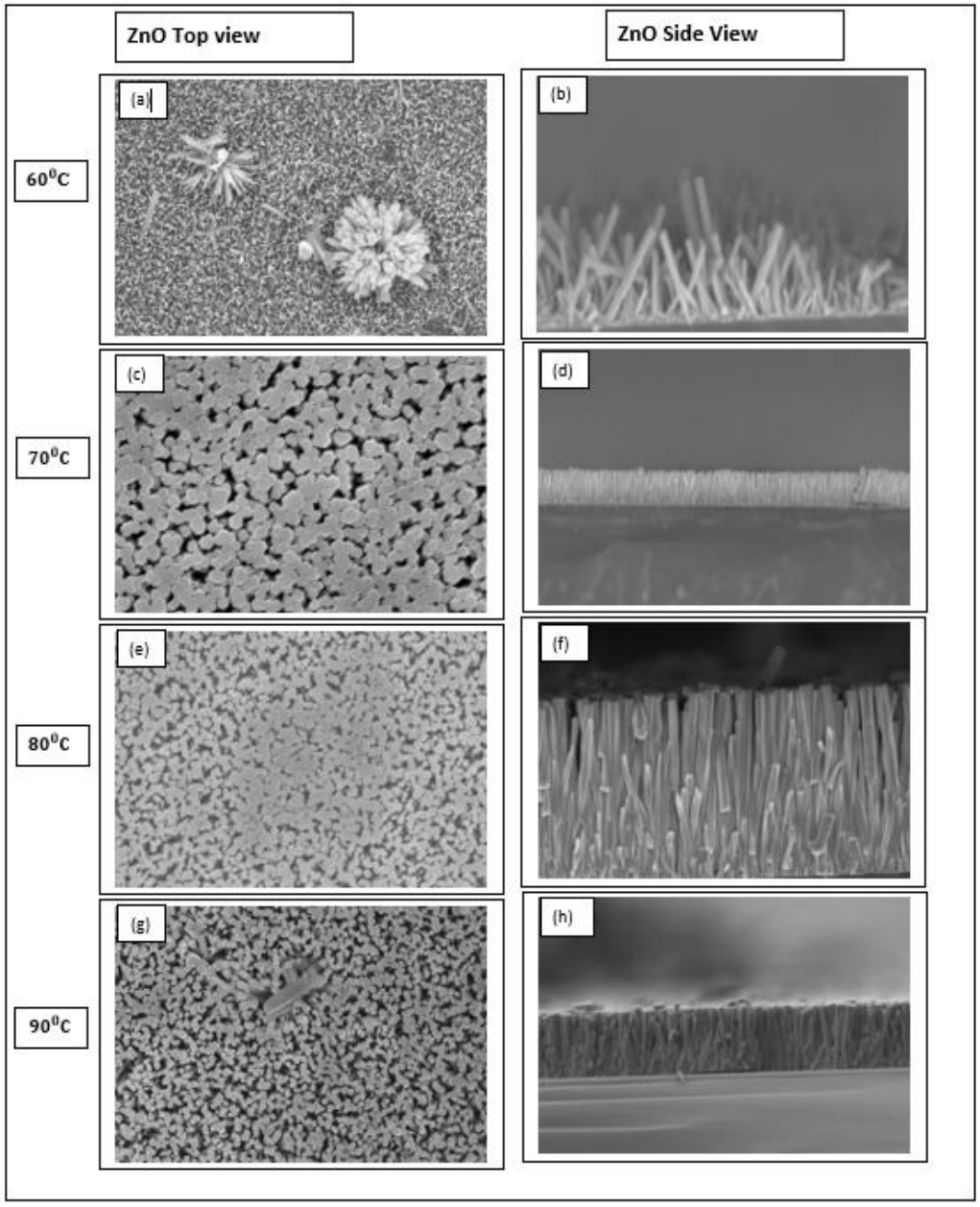


Figure 10: SEM images of all undoped ZnO nanorods samples grown at $60^0$C, $70^0$C, $80^0$C, $90^0$C with top view [(a), (c), (e ), (g)] and side view [(b), (d), (f), (h)]

Figure 10 shows all the SEM images of the nanorods grown at each temperature. It shows that nearly all the ZnO nanorods are perpendicularly oriented to the substrate regardless to the growth temperatures but not so much for $60^0$C. At $60^0$C, we can see only few nanorods are perpendicular

to the substrate. From the top view of nanorods it can be seen that all nanorods have hexagonal shape. Which suggests that all the nanorods grow along the [001] direction at various temperatures. The growth temperature has a great impact on the diameter, length and aspect ratio of the nanorods. At higher temperatures we have better uniformity, higher density, better orientation, wider and longer nanorods. One reason for this is that the decomposition rate of HMTA becomes faster at higher temperatures, producing a larger amount of $OH^-$ ions and increasing the nanorods growth role [54].

Table information of size of nanorods with SEM images

| Sample | Average diameter (nm) | Average length (nm) | Aspect ratio |
|---|---|---|---|
| ZnO $60^0$C | 68 | 372 | 5.47 |
| ZnO $70^0$C | 122 | 529 | 4.33 |
| ZnO $80^0$C | 136 | 1577 | 11.59 |
| ZnO $90^0$C | 158 | 1620 | 10.25 |

From table 1 we can see that diameter and length of nanorods increase as temperature is increases.

The aspect ratio at $70^0$C is smaller as compared to that found at higher temperatures. The average diameter increases from 68 nm to 158 nm and the length from 372nm to 1620 nm. This shows that the growth rate along [001] direction is very sensitive to temperature.

# 3. 3. Raman Spectroscopy

We have used micro-Raman spectroscopy, a technique of choice to examine the crystal structure of nanorods. Local Raman shifts were measured at room temperature using a Renishaw inVia micro-Raman system having a 532 nm excitation laser and no polarization detection in the 150-475 $cm^{-1}$ wavenumber range. The ability to collect Raman data from a small area reduces undesirable background signals and provides detailed structure information.

ZnO nanorods possess a wurtzite crystal structure with $C_{6\square}^{4}$ symmetry and two formula units in the primitive cell [12]. The optical phonon modes of ZnO nanorods are classified as $A_1$+ $E_1$+ $2E_2$ + $B_1$, where $A_1$ and $E_1$ are polar and they are split into longitudinal and transverse optical phonons. Non-polar phonons with $E_2$ symmetry show two different frequencies in the Raman spectrum, $B_1$

modes are Raman silent. $E_2$ phonon modes are described as $E_2(H)$ and $E_2(\mathrm{L})$ and are related to oxygen and zinc sub-lattices in the ZnO crystals [13].

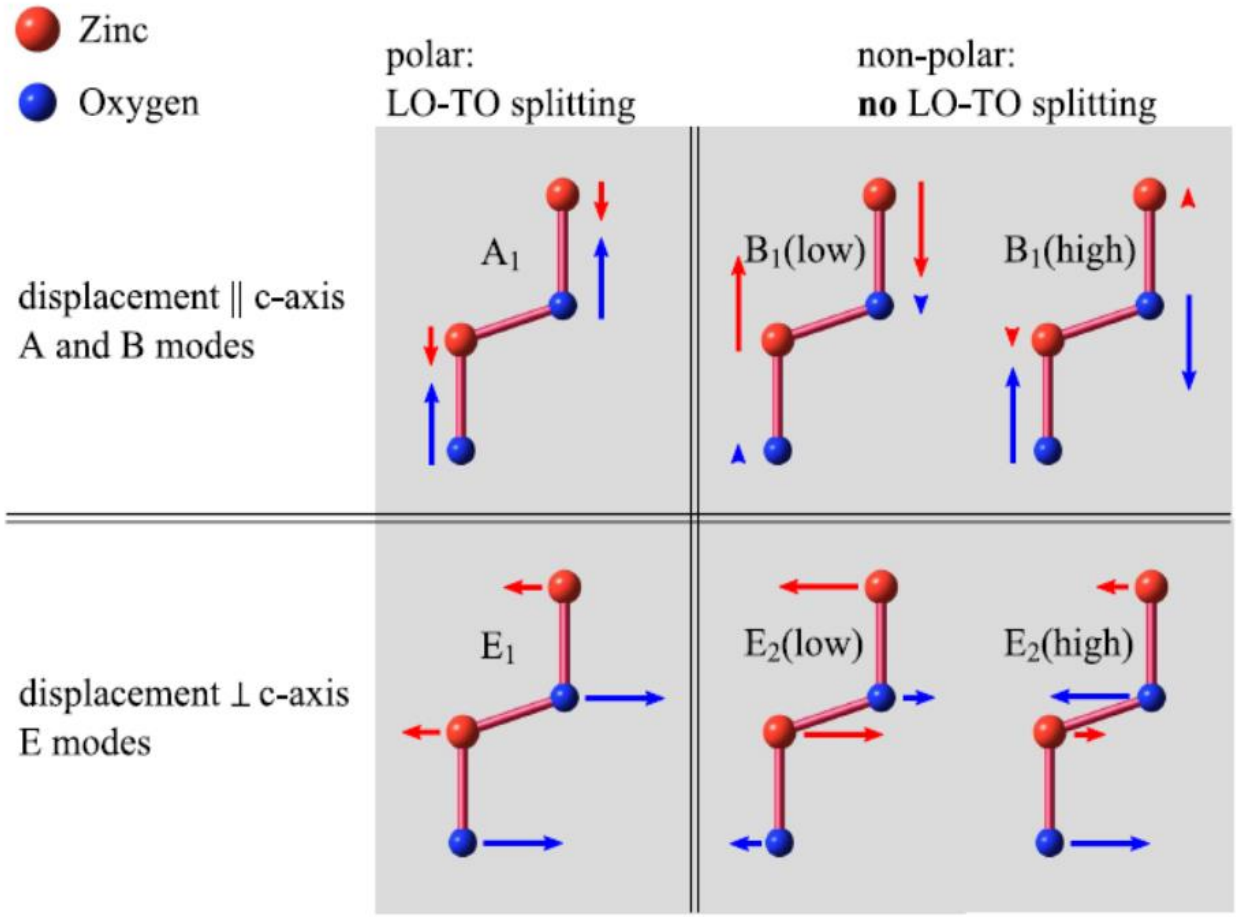


Figure 11: Possible vibrational modes in ZnO crystal (https://spectrum.library.concordia.ca/982460/)

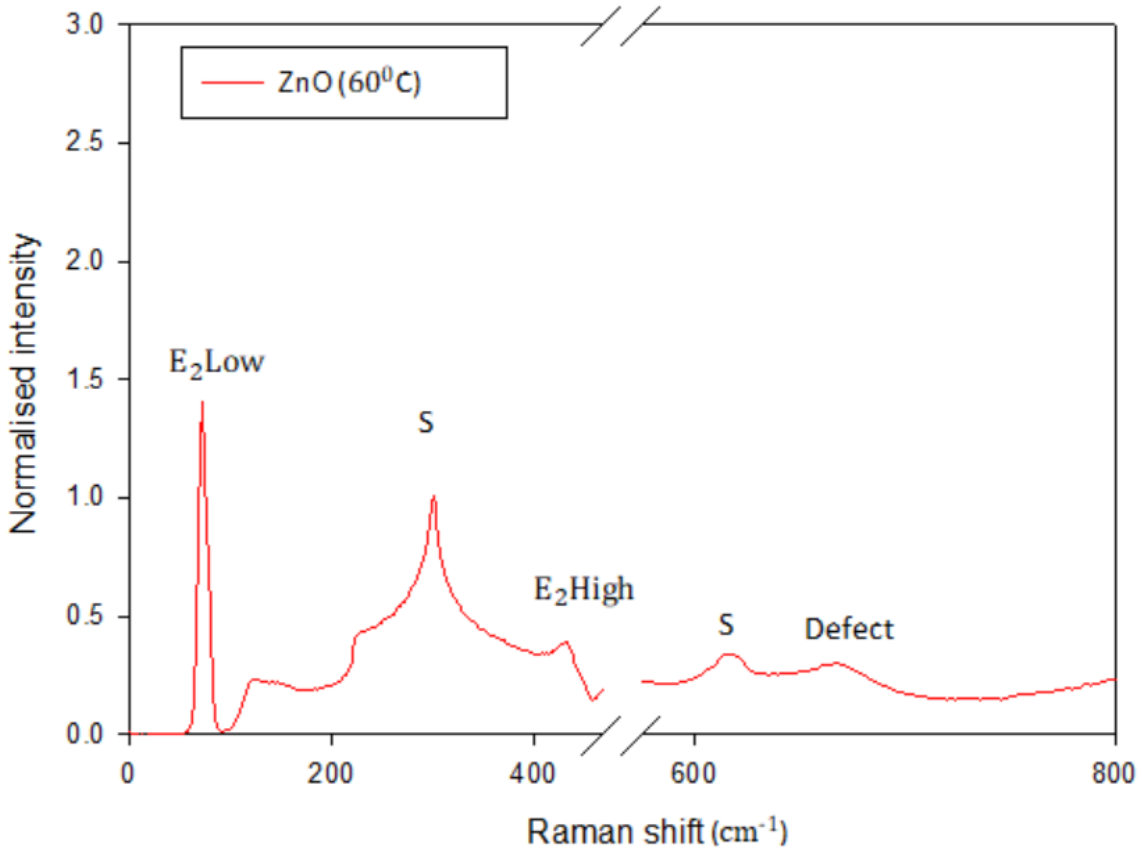


Figure 12: Micro-Raman spectra of ZnO nanorods grown at $60^0$C

Figure 12 shows the Raman spectra of ZnO nanorods grown at $60^0C$. Our results correspond to well known features of wurtzite ZnO with peaks corresponding to Raman active modes $A_1$, $E_1$, and $E_2$ [14]. Peak at 438 $cm^{-1}$ is assigned to the $E_2$(H) mode. This peak is evidence of wurtzite crystal orientation [15]. The S peak centered at 300 $cm^{-1}$ is due to the Silicon substrate. Raman scattering is an effective technique to find information about impurities in the ZnO nanocrystals. The propagation of $A_1$(TO) and $E_1$(LO)is perpendicular to c-axis and $A_1$(LO) and $E_1$(TO) propagate parallel to the c-axis [16]. $A_1$(TO) and $E_1$(TO) reflect the polar lattice bond, and $A_1$(LO) is attributed to oxygen vacancies and zinc interstitials [17]. The non-polar phonons with $E_2$ symmetry showed as two different frequencies in the Raman spectrum. $E_2$(L) modes are attributed

to vibration of oxygen atoms and $E_2$(H) are attribute to vibration of Zn sub-lattice [13]. Our results match with the well-known features of wurtzite ZnO, having $E_1$ and $E_2$ peaks.

The peaks centered at approximately 300 $cm^{-1}$, 621 $cm^{-1}$, 817$cm^{-1}$ are due to the silicon substrate. The peaks at 73$cm^{-1}$ and 434 $cm^{-1}$ are assigned to the $E_2$(L) and $E_2$(H) modes. As from figure 12 we can see that $E_2$(H) is not very sharp which means that the crystal orientation is not good. The broad $E_2$(H) peak reveals that less nanorods are perpendicular to the substrate. On the other hand, $E_2$(L) is very sharp. The broadening of the $E_2$(H) peak and sharp $E_2$(L) peak could be due to wurtzite lattice distortion. The small peak at 669 $cm^{-1}$ has been assigned to oxygen vacancies or zinc interstitials defect centers in the crystal lattice [22, 23].

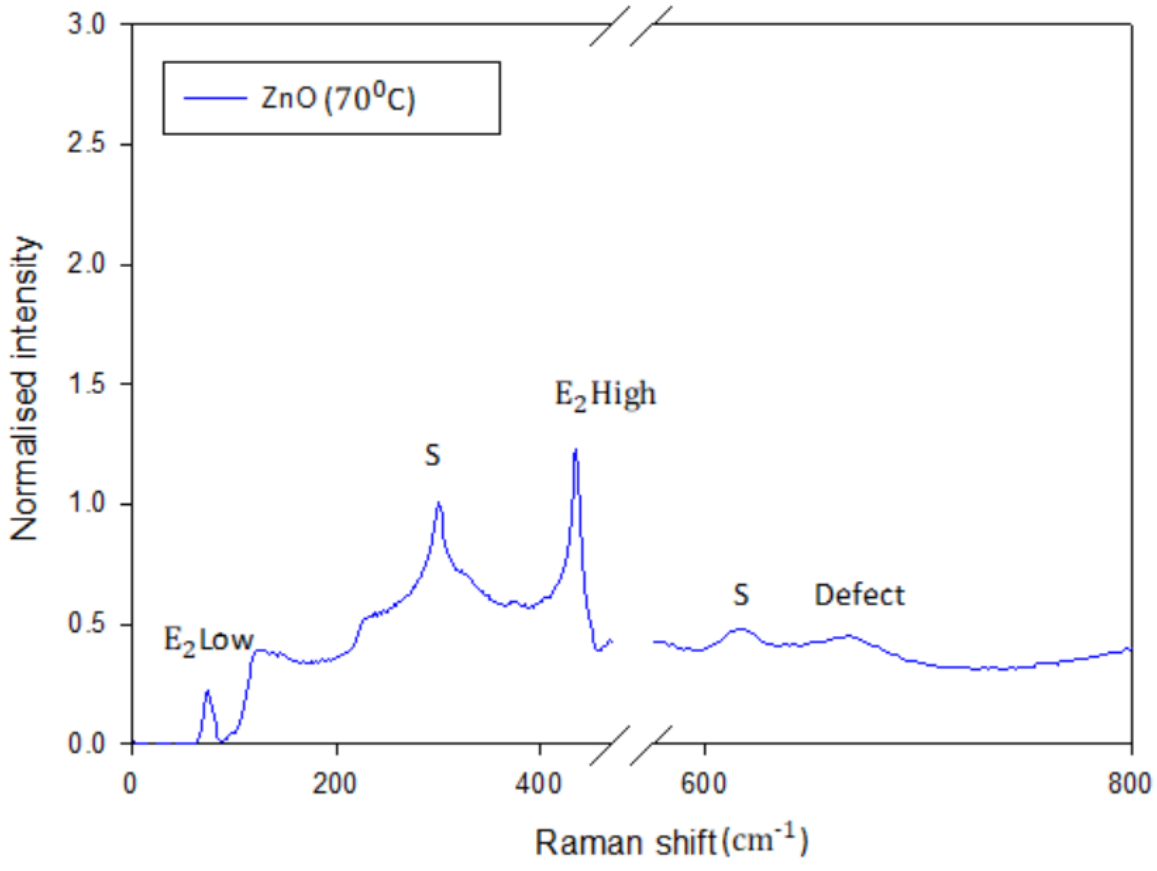


Figure 13 Micro-Raman spectra of ZnO nanorods grown at $70^0$C

Figure 13 shows that $E_2$(H) in nanorods grown at $70^0$C is much sharper as compared to those grown at $60^0C$, which means the crystal orientation was improved. The dominant sharp $E_2$(H) reveals that the nanorods are perpendicular to the substrate. $E_2$(L) is low. The broadening of $E_2$(L) peak and sharp $E_2$(H) peak are due to strong wurtzite lattice. The small peak at 663 $cm^{-1}$ has been assigned to oxygen vacancies or zinc interstitials defect centers in the crystal lattice.

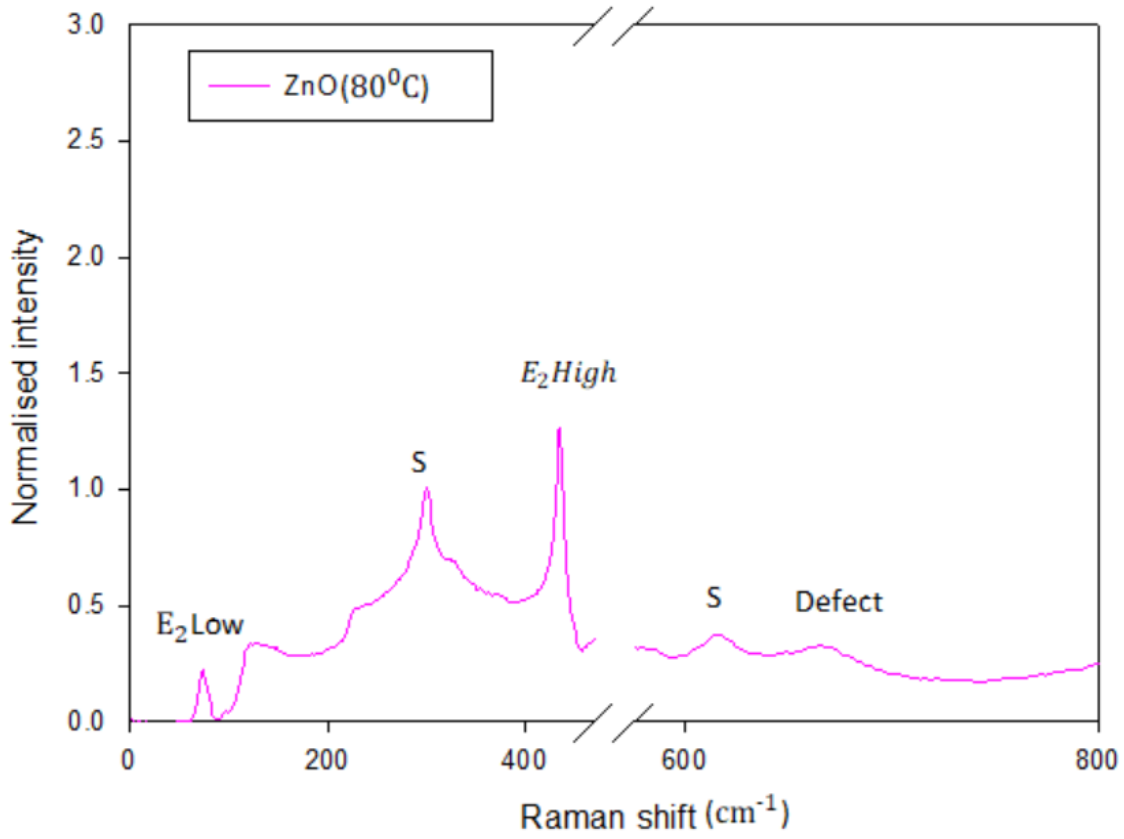


Figure 14: Micro-Raman spectra of ZnO nanorods grown at $80^0$C

From figure 14, it can be seen that for nanorods grown at $80^0$C that $E_2$(H) is sharp and $E_2$(L) is

low, which means that the crystal orientation is almost the same at $70^0$C and $80^0$C. The sharp $E_2$(H) is evidence of strong wurtzite crystal orientation and demonstrates that the overall crystal structure of ZnO is much affected by the temperature increment from $70^0$C to $80^0$C.

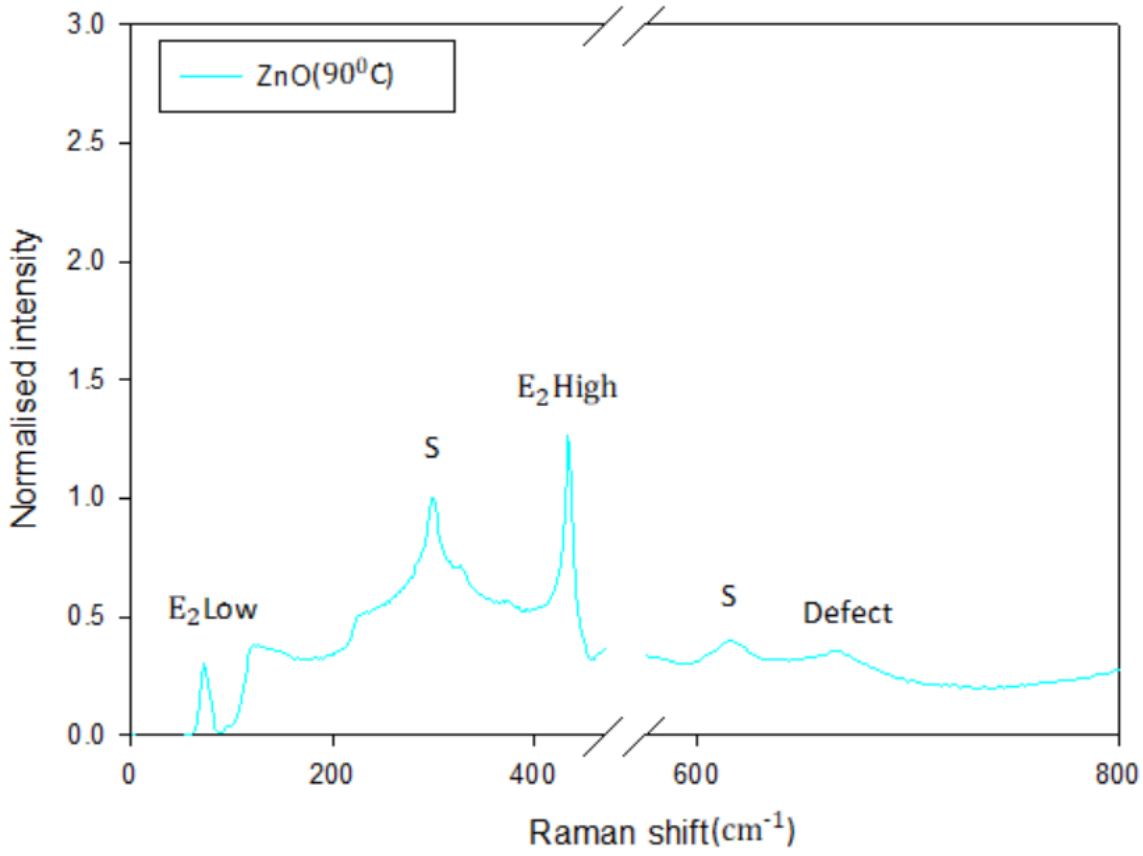


Figure 15: Micro-Raman spectra of ZnO nanorods grown at $90^0$C

Figure 15 shows that for nanorods grown at $90^0$C $E_2$(H) is sharp and $E_2$(L) is low, which means that the crystal orientation is almost same as at $70^0$C and $80^0$C. The sharp $E_2$(H) is evidence of strong wurtzite crystal orientation.

Table 2: Experimental results of the active modes of undoped ZnO nanorods grown at different temperatures

| **Sample** | **$E_2$(H) Peak($cm^{-1}$)** | **$E_2$(L) Peak ($cm^{-1}$)** | **Defects (Peak)($cm^{-1}$)** | **Amplitude of defect peak** |
|---|---|---|---|---|
| ZnO $60^0$C | 431.52 | 72.29 | 651.06 | 0.32 |
| ZnO $70^0$C | 434.62 | 74.03 | 658.55 | 0.36 |
| ZnO $80^0$C | 434.91 | 73.77 | 663.46 | 0.29 |
| ZnO $90^0$C | 434.34 | 73.13 | 663.12 | 0.22 |

We can see from the table that when growth temperature increases from $60^0$C to $70^0$C, the defect peak which is around 663($cm^{-1}$) increases in amplitude. When the temperature increases to $80^0$C and $90^0$C the amplitude of the defect peak start to decrease, which means higher temperature samples have less defects than those grown at low temperatures. The very small shifts of the $E_2$(H) and $E_2$(L) peaks (< 2%) gives us confidence about the wurtzite structure of the nanorods.

# 3.4. Photoluminescence

PL spectroscopy is a technique used to investigate impurities, dopant or crystal defects in semiconductor crystals and more, such as their electronic structure. To study the influence of growth temperature on the optical properties of nanorod arrays PL measurements were conducted at room temperature.

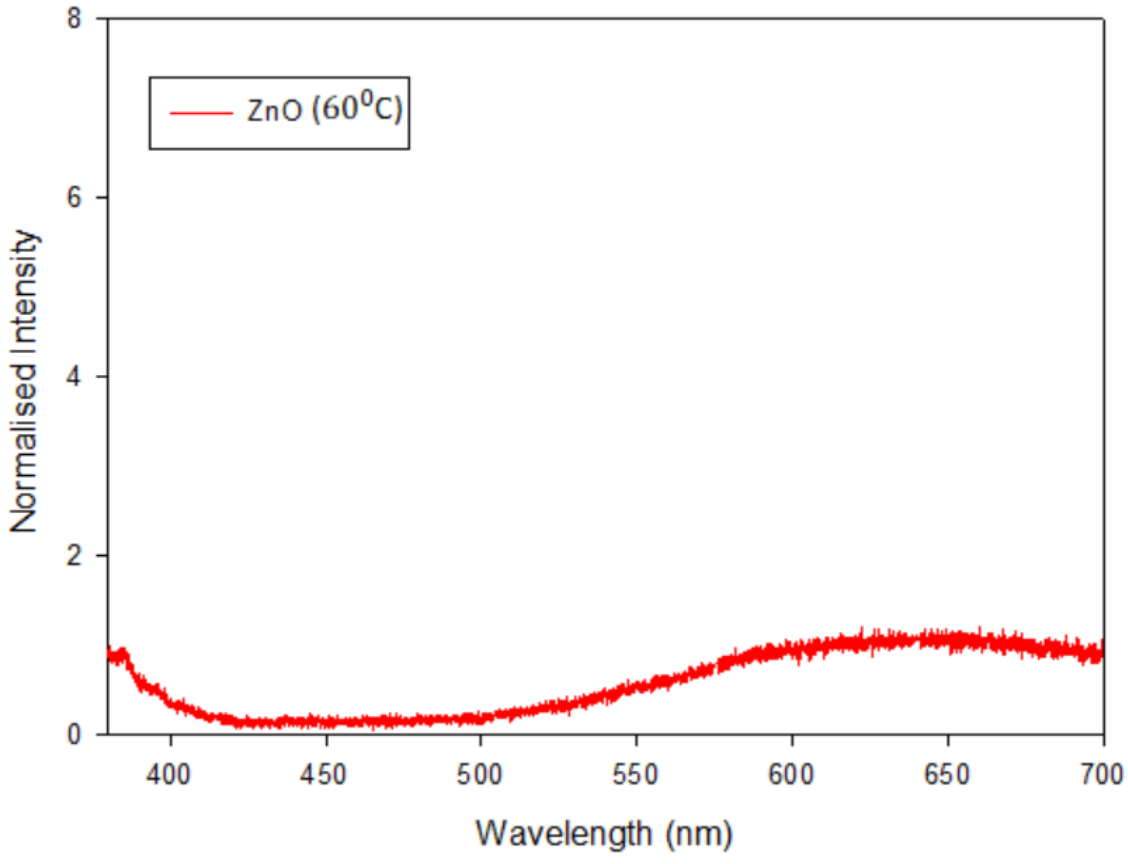


Figure 16: Room temperature photoluminescence of the ZnO nanorods grown at 60$^0$C on silicon substrate

Room- temperature micro-PL spectroscopy was performed with an excitation wavelength of 369 nm in air. To study our sample, we have used a home built micro-PL setup at room temperature. An excitation wavelength of 369 nm was used and is incident on the sample with glancing angle. You can see the micro-Pl spectra of the ZnO nanorods grown at $60^0$C temperature in a figure 16. A narrow peak at 384 nm was observed, which is known as near band edge (NBE) emission. NBE emission is mainly attributed to free exciton recombination in the ZnO lattice [18]. There is broad peak around 570 nm to 700 nm that is known as defect peak. The defect emission peak corresponds to green, yellow and red emission in ZnO nanorods which originates from different types of defects centers [20]. Defects could be oxygen vacancies, ZnO interstitials etc., etc [19] [21]. We have used the normalised intensity of NBE emission peak in all the PL spectrum.

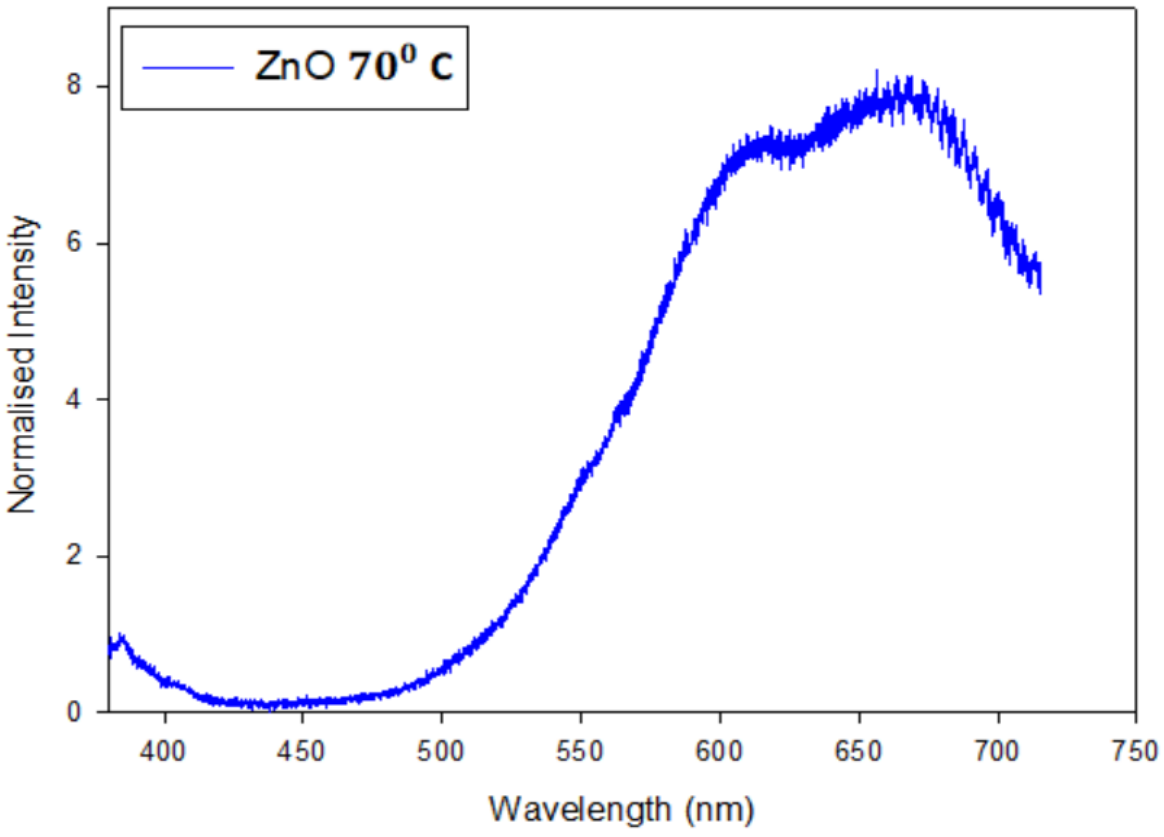


Figure 17: Room temperature photoluminescence of the ZnO nanorods grown at $70^0$C on silicon substrate

Figure 17 shows the room temperature photoluminescence spectra of ZnO nanorods grown at $70^0$C. We can see that at $70^0$C the amplitude of defect peak abruptly increases. That means we have many more defects.

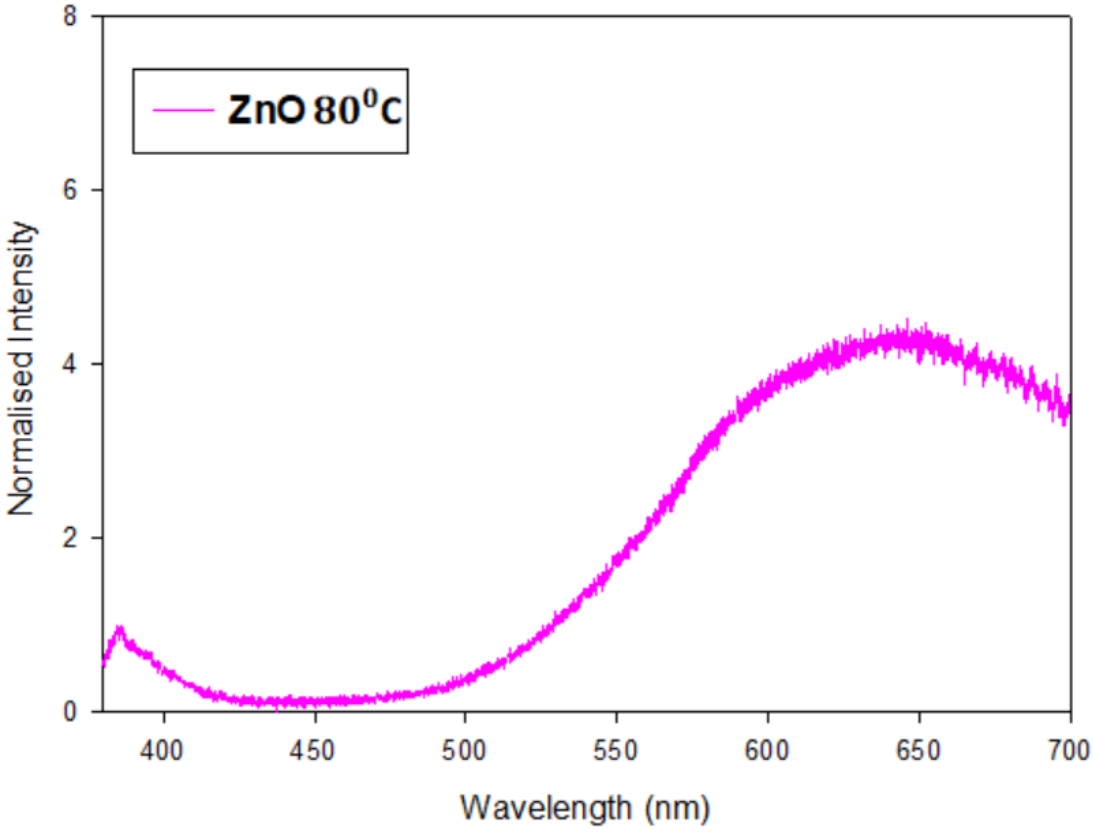


Figure 18: Room temperature photoluminescence of the ZnO nanorods grown at $80^0$C on silicon substrate

The spectra of ZnO nanorods grown at $80^0$C in figure 18 shows that the defect peak at this temperature starts decreases in amplitude compared to the defect emission peak at $70^0$C.

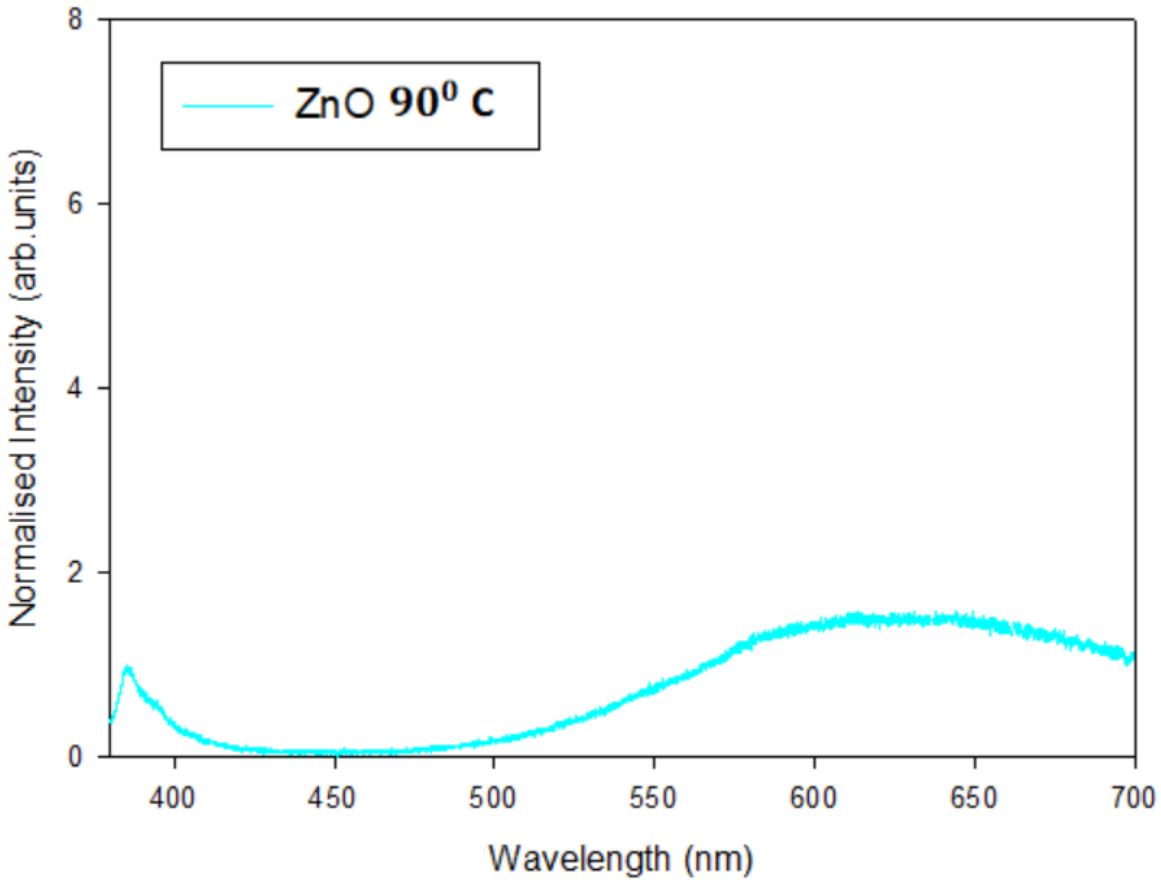


Figure 19: Room temperature photoluminescence of the ZnO nanorods grown at $90^0$C on silicon substrate

Figure 19 shows the room temperature PL spectra of ZnO nanorods grown at $90^0$C. The defect peak becomes smaller than that at $80^0$C.

Table 3: Experimental results of the PL spectra of undoped ZnO nanorods grown at different temperatures

| Sample | Defect emission area | Defect emission FWHM | Defect emission peak amplitude |
|---|---|---|---|
| ZnO $60^0$C | 221.68 | 191.37 | 1.08 |
| ZnO $70^0$C | 1331.17 | 313.53 | 7.34 |
| ZnO $80^0$C | 827.23 | 259.82 | 4.97 |
| ZnO $90^0$C | 284.62 | 236.28 | 1.73 |

We can see from Table 3 that from $60^0$C to $70^0$C, defect emission area, defect emission FWHM, defect emission peak amplitude increases. After that at $80^0$C and $90^0$C, these factors start decreasing. We can say that at $70^0$C, ZnO nanorods have more defects.

# 3.5. ESR Spectroscopy

ESR is a most powerful technique which reveals the presence of defect states of materials. The outcome of ESR characterisation is shown in figure 20. ZnO is expected to be diamagnetic.

For ZnO nanorods grown at $60^0$C, a signal was observed at g = 1.96 which is attributed to core defects.

This signal can be assigned to unpaired electrons trapped on oxygen vacancies, which is reported to the result from shallow donor centers such as ionised impurity atoms in the crystal lattice of ZnO [39-41].

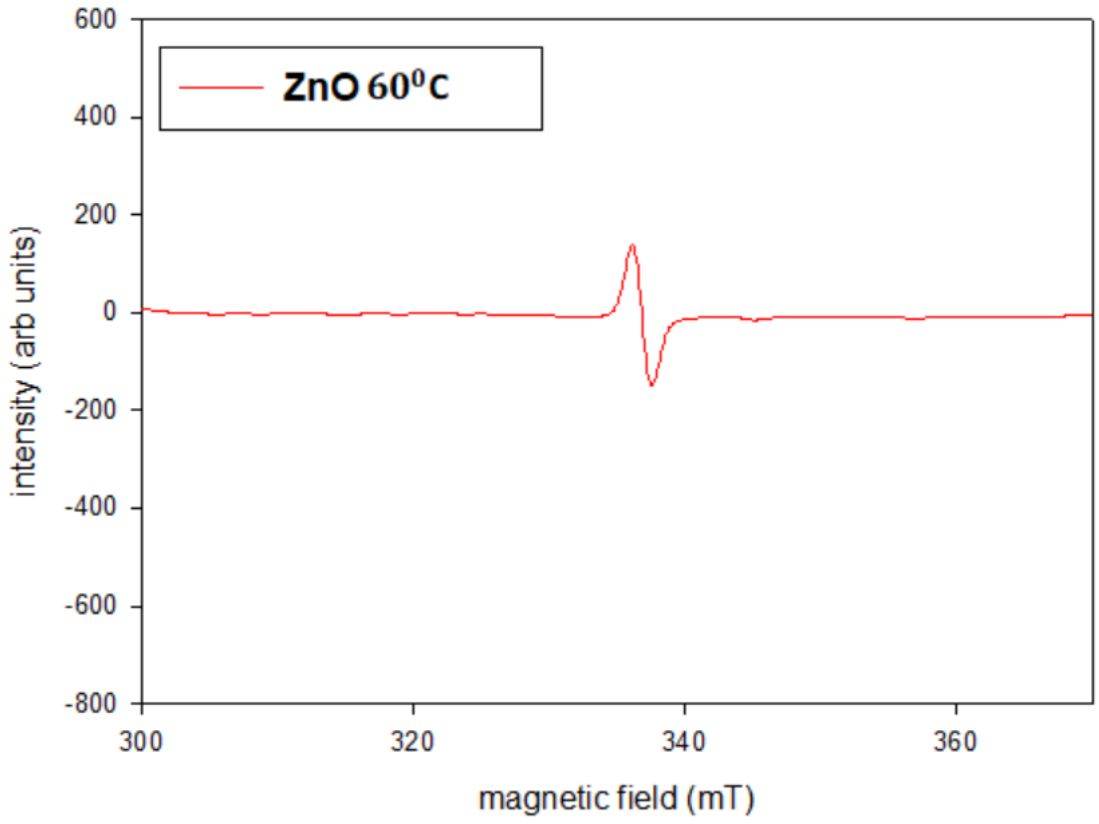


Figure 20: ESR spectrum of ZnO nanorods grown at $60^0$C

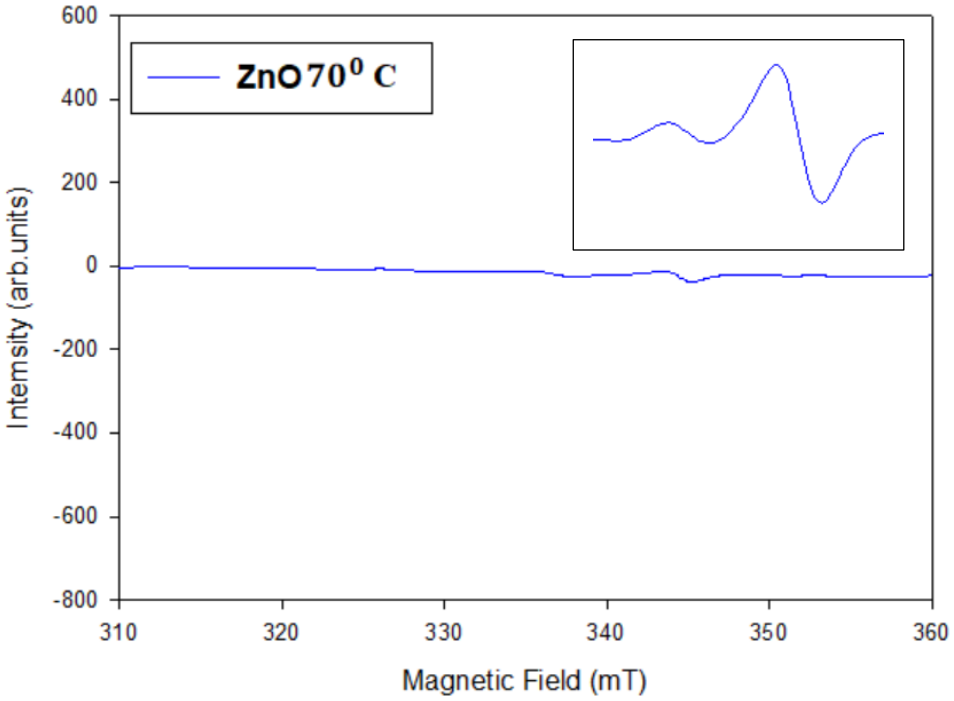


Figure 21: ESR spectrum of ZnO nanorods grown at $70^0$C

From figure 21, we can see that the ESR spectra of ZnO nanorods grown at $70^0$C gives one additional line at low field with g-factor = 2.00. this reveals surface defects close to the free electron value (g = 2.0023) arising from singly ionized oxygen vacancies ($V_O{}^+$), electron confined in doubly ionized oxygen vacancy states ($V_O{}^{++}$) and forming deep donor paramagnetic centers [37, 38, 42, 43]. The signal is very weak for surface and core defects as compared to other samples.

The surface line with the oxygen vacancy came from the observation of hyperfine interaction with Zn neighbours of the vacancy [58, 59]. The core line is associated with electrons in the conduction or in a donor bond [60].

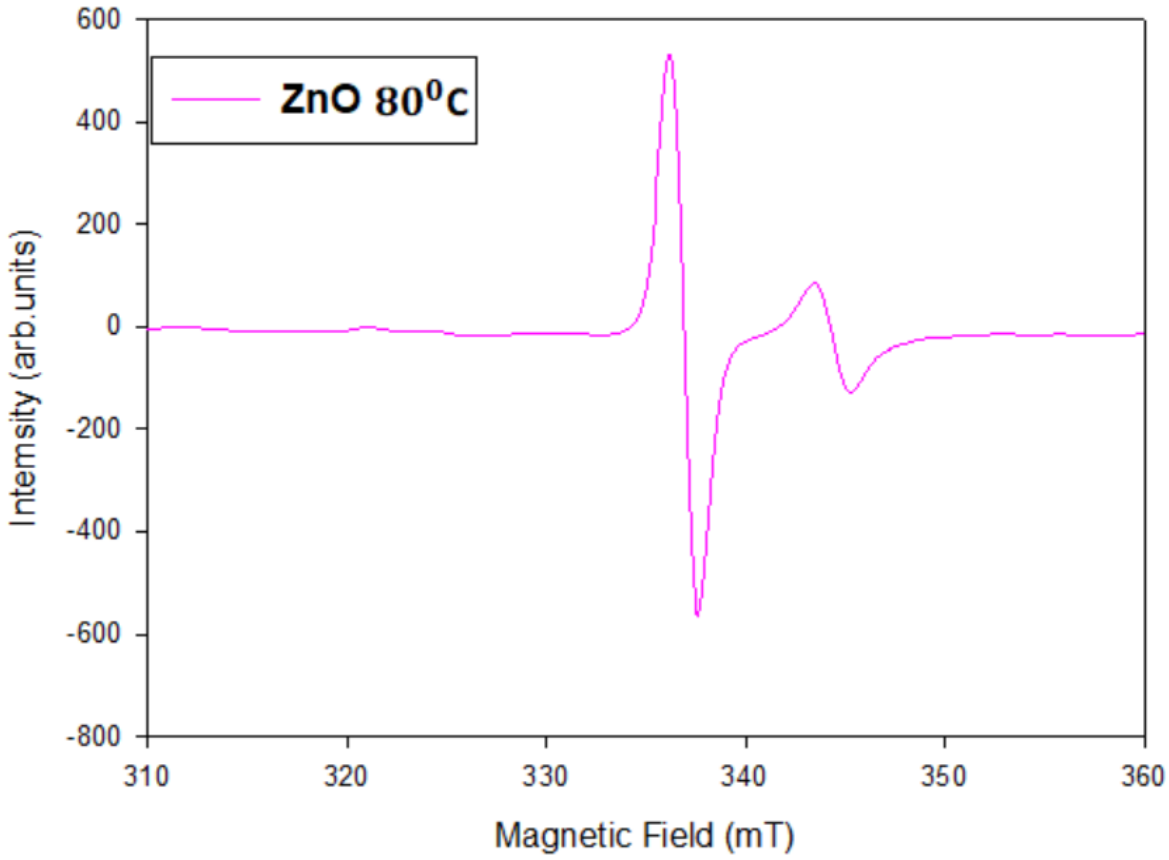


Figure 22: ESR spectrum of ZnO nanorods grown at $80^0$C

From figure 22 we see that the ESR spectra of ZnO nanorods grown at $80^0$C has two clean ESR signals, one at low magnetic field (surface defect) with g factor = 2.00 and a second one at high magnetic field (core defect) with g = 1.96.

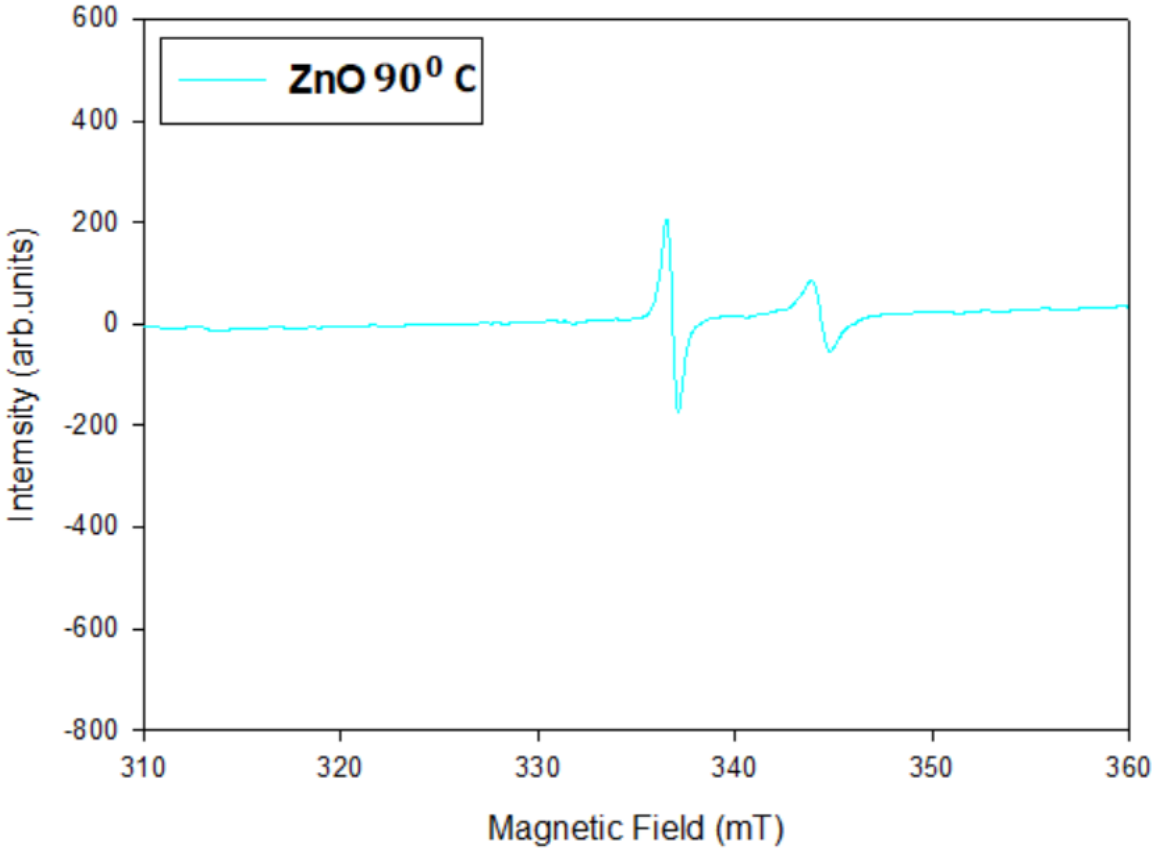


Figure 23: ESR spectrum of ZnO nanorods grown at $90^0$C

From figure 23 we see that ESR spectra of ZnO nanorods grown at $90^0$C have two ESR signals, one at low magnetic field (surface defect) with g factor = 2.00 and a second one at high magnetic field (core defect) with g = 1.96, same as ZnO nanorods grown at $80^0$C.

Table 4: Experimental results of ESR spectra of ZnO nanorods at different temperatures ($60^0$C, $70^0$C, $80^0$C, $90^0$C)

| Sample | Line width (core defects) | g-factor | Line width (surface defects) | g-factor |
|---|---|---|---|---|
| ZnO $60^0$C | 1.58 | 1.96 | No line | |
| ZnO $70^0$C | 4.02 | 1.96 | 1.89 | 2.00 |
| ZnO $80^0$C | 1.40 | 1.96 | 1.7 | 2.00 |
| ZnO $90^0$C | 0.58 | 1.96 | 0.93 | 2.00 |

As you can see from table 4 that when the temperature is increased from $60^0$C to $70^0$C, the line width of ESR signal for core defects and surface defects is increased. At $80^0$C and $90^0$C the line width for core and surface defects decreases. As the line width is larger, we have larger defect concentration. Smaller the line width, then there is less concentration of defects.

# Chapter 4

# Systematic study of Mn-doped ZnO nanorods grown at different temperatures

## 4.1. Introduction

In this chapter, we will discuss about our Mn- doped ZnO nanorods. 1% of Mn is used to dope the ZnO nanorods. We have samples grown at different temperatures: $60^0$C, $70^0$C, $80^0$C, and $90^0$C. We have used different techniques to characterize the Mn-doped ZnO nanorods like SEM, Raman Spectroscopy, Photoluminescence spectroscopy, and EPR spectroscopy.

According to Mandal et al. [44] $Mn^{2+}$ and $Co^{2+}$ are the two most soluble cations in ZnO nanocrystals. When using a hydrothermal method, Mn is a good candidate to be doped into ZnO nanorods where these different temperatures are expected to incorporate the dopant ions into the host lattice. Doping of ZnO by $Mn^{2+}$ is one of the most significant approach towards the

development of ferromagnetic diluted magnetic semiconductors (DMS) with a Curie temperature above room temperature. [45]. Ahmed et al found that undoped ZnO oxygen gas sensitivity can be improved by adding $Mn^{2+}$[56]. By using common chemical-based methods such as chemical vapour deposition [46], chemical bath deposition [47] and solution growth method, the successful incorporation of Mn into ZnO has been reported before. If we compare the low temperature hydrothermal growth method with other growth methods, the hydrothermal method stands out due to its large scale and low-price device fabrication. It is a big challenge to achieve the incorporation of $Mn^{2+}$ into ZnO with a hydrothermal growth method at these growth temperatures because of the strong Mn-O bonding [55]. Therefore, the achievable doping percentage of $Mn^{2+}$ in ZnO crystals using solution growth methods is expected to be lower than the nonequilibrium high temperature methods like CVD. In the past, to handle this problem, high-temperature solution based $Mn^{2+}$ doping of ZnO nanorods has been done. The nanorods grown at these temperatures were randomly aligned to the substrate and they were not uniform in size. Singh et al [47] reported Mn-doped ZnO nanorods at low temperature ($65^0$C) on a seeded glass substrate. The alignment of nanorods was improved but their uniformity was hindered possibly because of clusters formed by a combination of coated MnO and ZnO nanoparticles. Panigrahy et al [48] reported that random alignment of nanorods could be due to the non-treated substrates. Similarly, in other reports with hydrothermal preparation methods Mn-doped ZnO nanorods have shown lack of uniformity due to size dispersion of seed nanoparticles [49, 50]. Therefore, the challenge of growth of Mn-doped ZnO nanorods under mild conditions without affecting morphology and uniformity is still unsolved.

In this chapter, the structural, and optical properties of Mn-doped Zno nanorods synthesized by a hydrothermal method at different temperatures ($60^0$C, $70^0$C, $80^0$C, $90^0$C) will be discussed.

# 4.2. Morphology

SEM images of ZnO nanorods doped with Mn (1%) grown at $60^0$C are shown in figure 29.

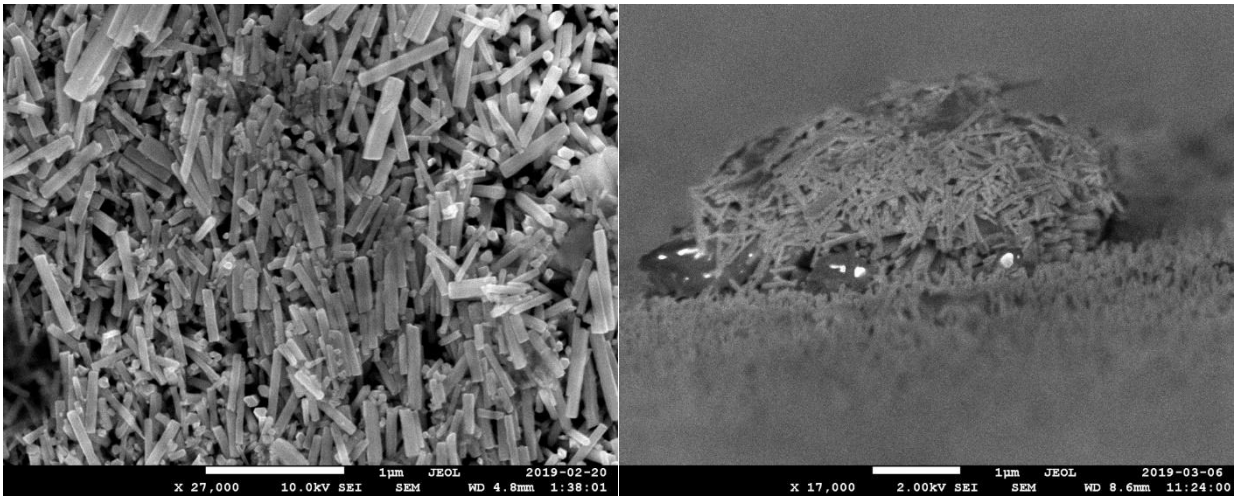


Figure 24: SEM images of doped ZnO (Mn 1%) nanorods grown at $60^0$C. Left is image of top view and right is image of side view.

The nanorods have hexagonal shape. Their average length is 69 nm and their average diameter is 803 nm. We saw the majority of ZnO (Mn 1%) nanorods are not vertically aligned to the substrate at $60^0$C.

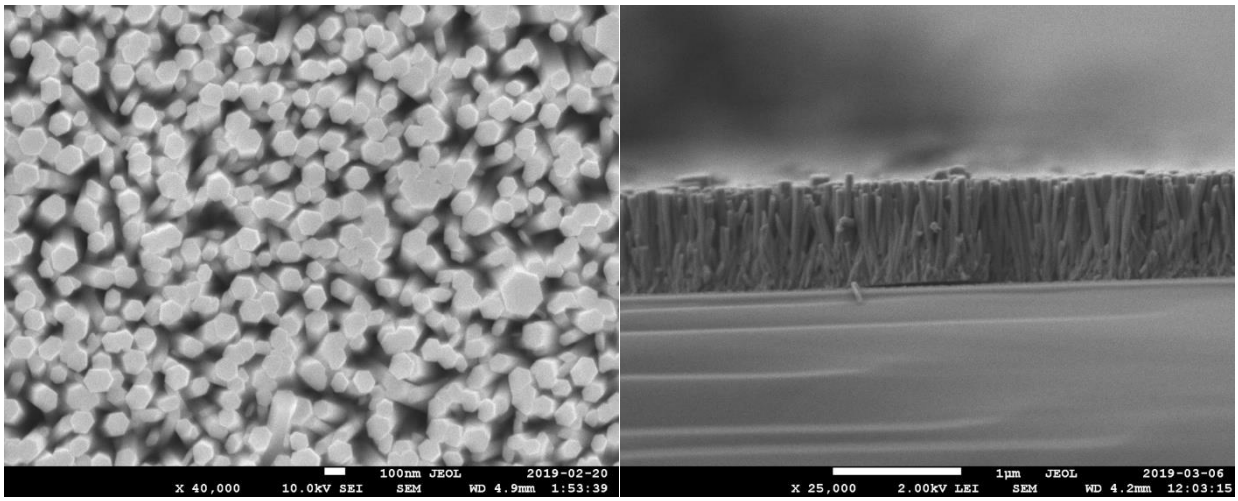


Figure 25: SEM images of doped ZnO (Mn 1%) nanorods grown at $70^0$C. Left is image of top view and right is image of side view.

ZnO (Mn 1%) nanorods grown at $70^0$C are shown in figure 30. We can see that the average length of the nanorods is increased as compared to the average length at $60^0$C. The average diameter also increased. The orientation of nanorods is really improved at $70^0$C and the nanorods are more uniform. Most of the nanorods are oriented perpendicular to the substrate.

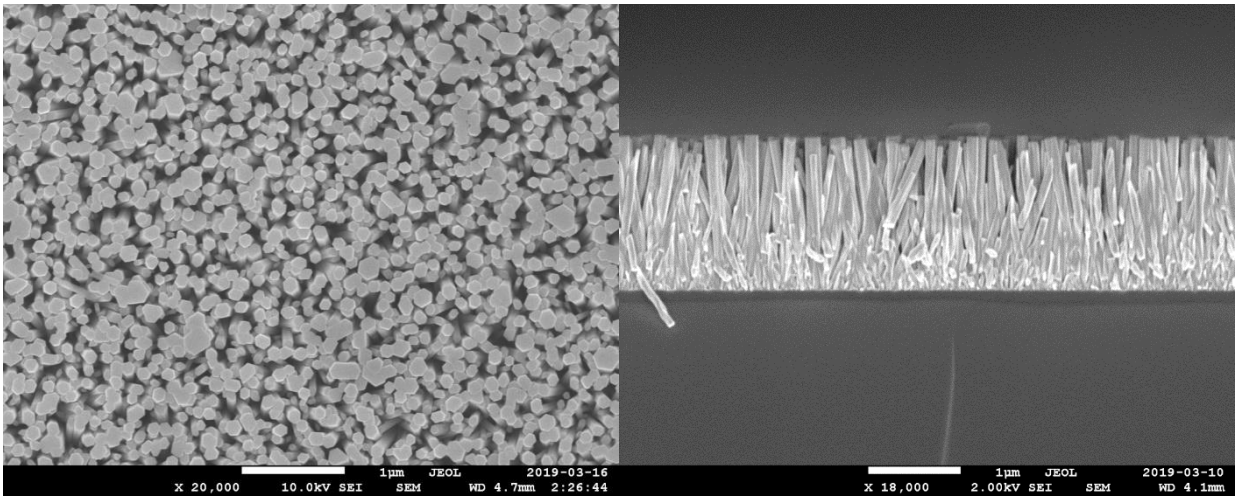


Figure 26: SEM images of doped ZnO (Mn 1%) nanorods grown at $80^0$C. Left is image of top view and right is image of side view.

Figure 26 shows that nanorods grown at $80^0$C are dense as compared to $60^0$C and $70^0$C. The average length and diameter of the nanorods increased to 119 nm and 1622 nm respectively.

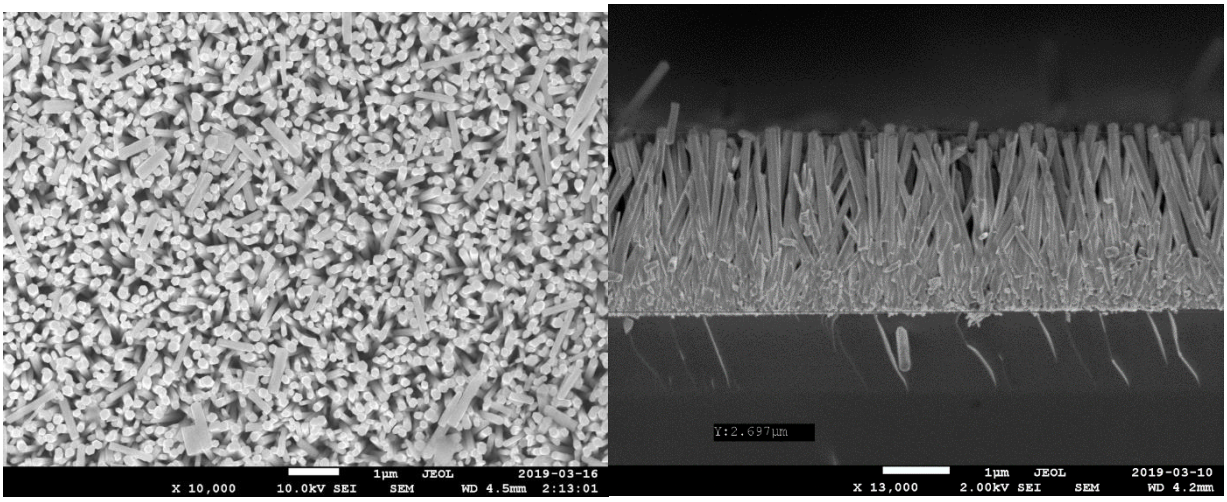


Figure 27: SEM images of doped ZnO (Mn 1%) nanorods grown at $90^0$C. Left is image of top view and right is image of side view.

At $90^0$C, the average diameter of nanorods is 150 nm and the average length is 2782 nm a further increase. The orientation of nanorods stays the same at temperatures higher than $70^0$C.

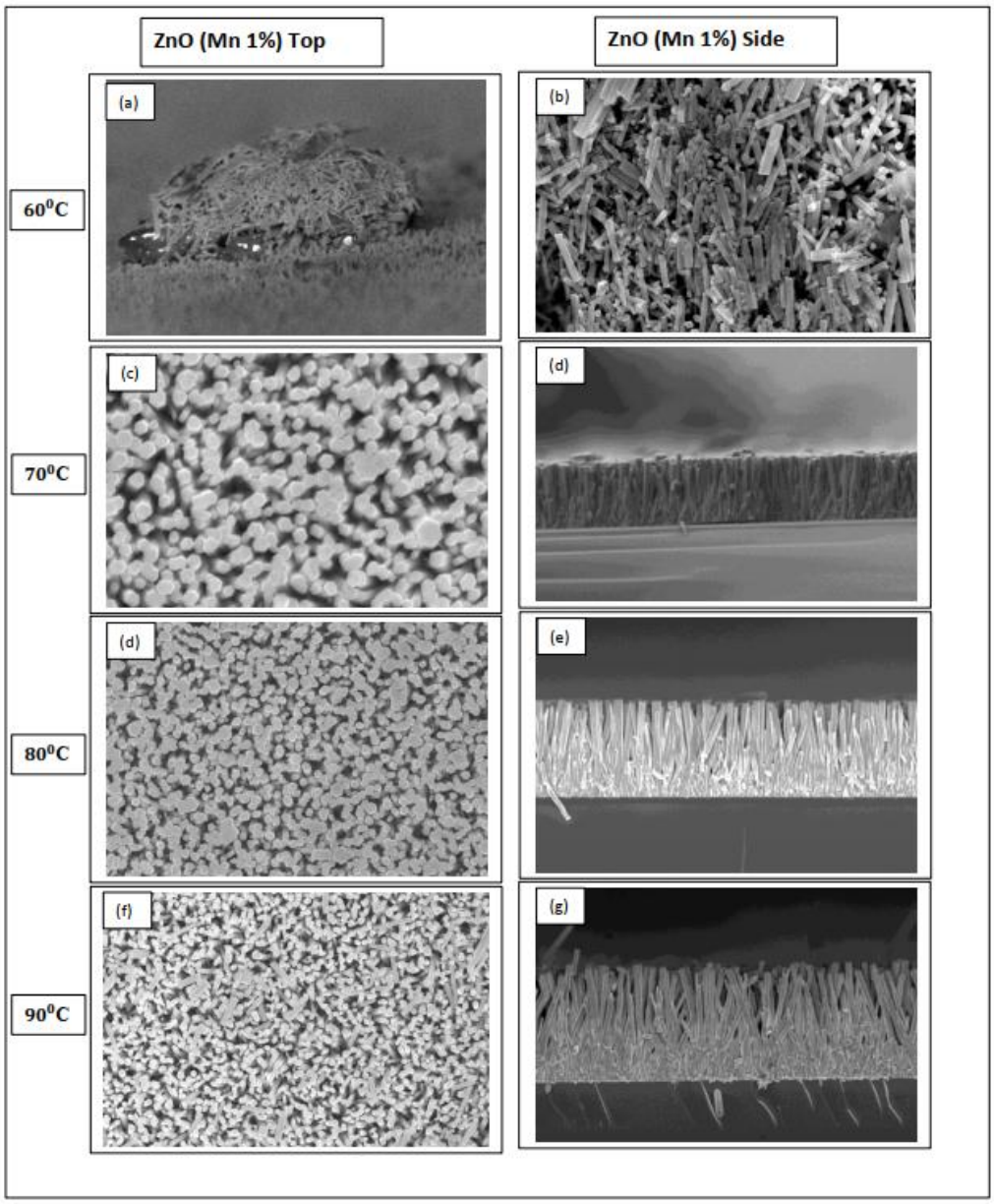


Figure 28: SEM images of all Mn-doped ZnO nanorods samples grown at $60^0$C, $70^0$C, $80^0$C, $90^0$C with top view [(a), (c), (e ), (g)] and side view [(b), (d), (f), (h)]

Figure 28 show all the SEM images of nanorods grown at each temperature together. It shows that nearly all the ZnO nanorods are perpendicularly oriented to the substrate regardless to the growth temperatures except the Mn-doped ZnO sample grown at $60^0$C. At $60^0$C, we can see that only few nanorods are perpendicular to the substrate. From the top view of the nanorods it is revealed that all nanorods have hexagonal shape. This suggests that all the nanorods grow along [001] direction at various temperatures. By increasing the growth temperatures, the diameter, length and aspect ratio of the nanorods increase. At higher temperatures we have better uniformity, higher density, better orientation, one reason for this is that the decomposition rate of HMTA becomes longer at higher temperatures, producing a larger amount of $OH^-$ ions and increasing the nanorods growth role [54].

Table 5: Information of size of nanorods with the SEM images

| Sample | Average Diameter (nm) | Height (nm) | Aspect ratio |
|---|---|---|---|
| ZnO (Mn 1%) $60^0$C | 69 | 803 | 11.63 |
| ZnO (Mn 1%) $70^0$C | 115 | 861 | 7.48 |
| ZnO (Mn 1%) $80^0$C | 119 | 1622 | 13.63 |
| ZnO (Mn 1%) $90^0$C | 150 | 2782 | 18.54 |

From table 5 we can see that diameter and length of nanorods increase as the growth temperature is increased. The aspect ratio at $70^0$C is smaller compared to other temperatures.

# 4. 3. Raman Spectroscopy

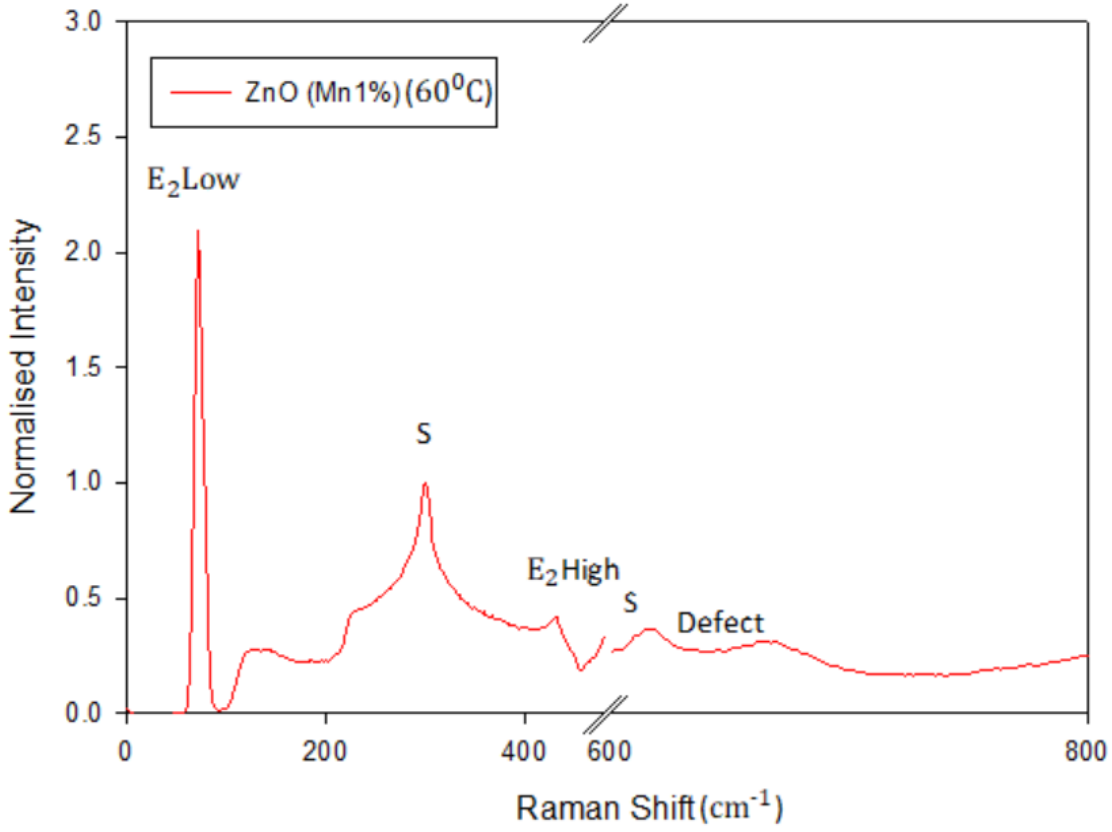


Figure 29: Micro-Raman spectra of ZnO nanorods grown at $60^0$C

Figure 29 shows the Raman spectra of Mn (1%) doped ZnO nanorods grown at $60^0$C. There we can see that $E_2$(H) is not very sharp, which means that the crystal orientation is not good. A broad

$E_2$(H) reveals that less nanorods are perpendicular to the substrate. On the other hand, $E_2$(L) is very sharp. The small peak at 669 $cm^{-1}$ has been assigned to the oxygen vacancies or zinc interstitials defect centers in crystal lattice.

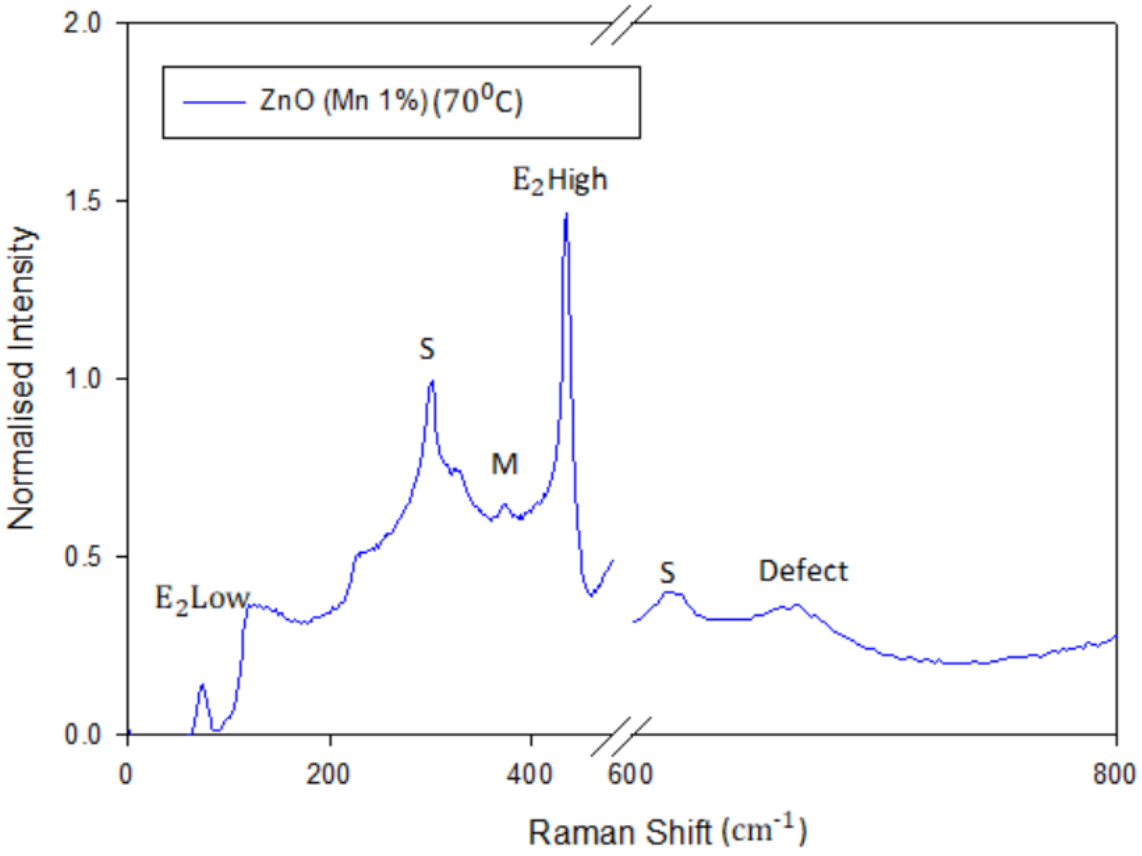


Figure 30: Micro-Raman spectra of ZnO nanorods grown at $70^0$C

Figure 30 that $E_2$(H) is increased compared to $60^0$C, which means that the crystal orientation was significantly improved. The dominant sharp $E_2$(H) reveals that the nanorods are perpendicular to the substrate. $E_2$(L) is very low. The low $E_2$(L) peak and sharp $E_2$(H) peak is due to a clear wurtzite

lattice. The small peak at 663 $cm^{-1}$ has been assigned to the oxygen vacancies or zinc interstitials defect centers in crystal lattice. The M peak is due to the non-flat surface of the nanorods.

The M peaks located at approximately 330 $cm^{-1}$ are known as Frohlich-type vibrational modes due to the multi-phonon scattering processes. Multi-phonon scattering can be due to quantum confinement effects in the nanorods sharp tips.

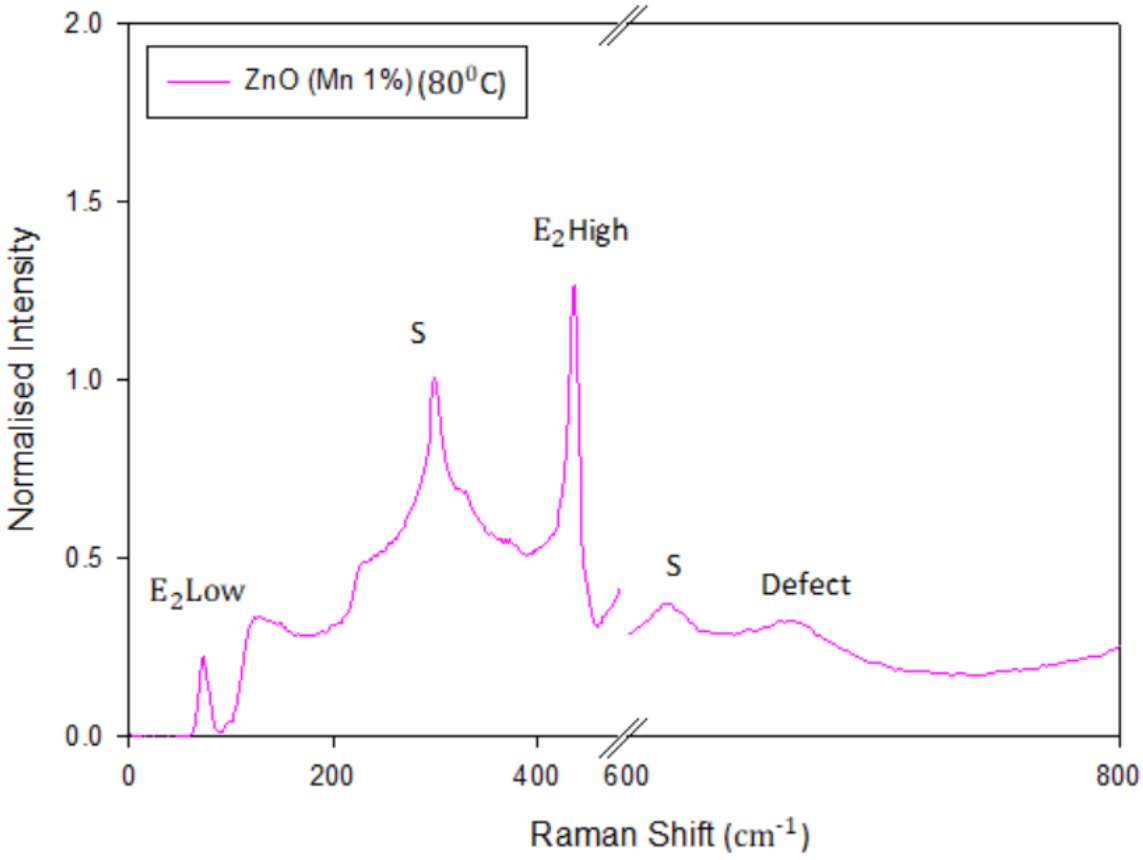


Figure 31: Micro-Raman spectra of ZnO nanorods grown at $80^0$C

In figure 31 we see that $E_2$(H) is sharp and strong while $E_2$(L) is low. The magnitude of $E_2$(H) is slightly less than the magnitude of $E_2$(H) of $70^0$C growth temperature samples. That means that the crystal orientation is almost the same as at $70^0$C and $80^0$C. The disappearance of the M peak is due to the flat surface of nanorods.

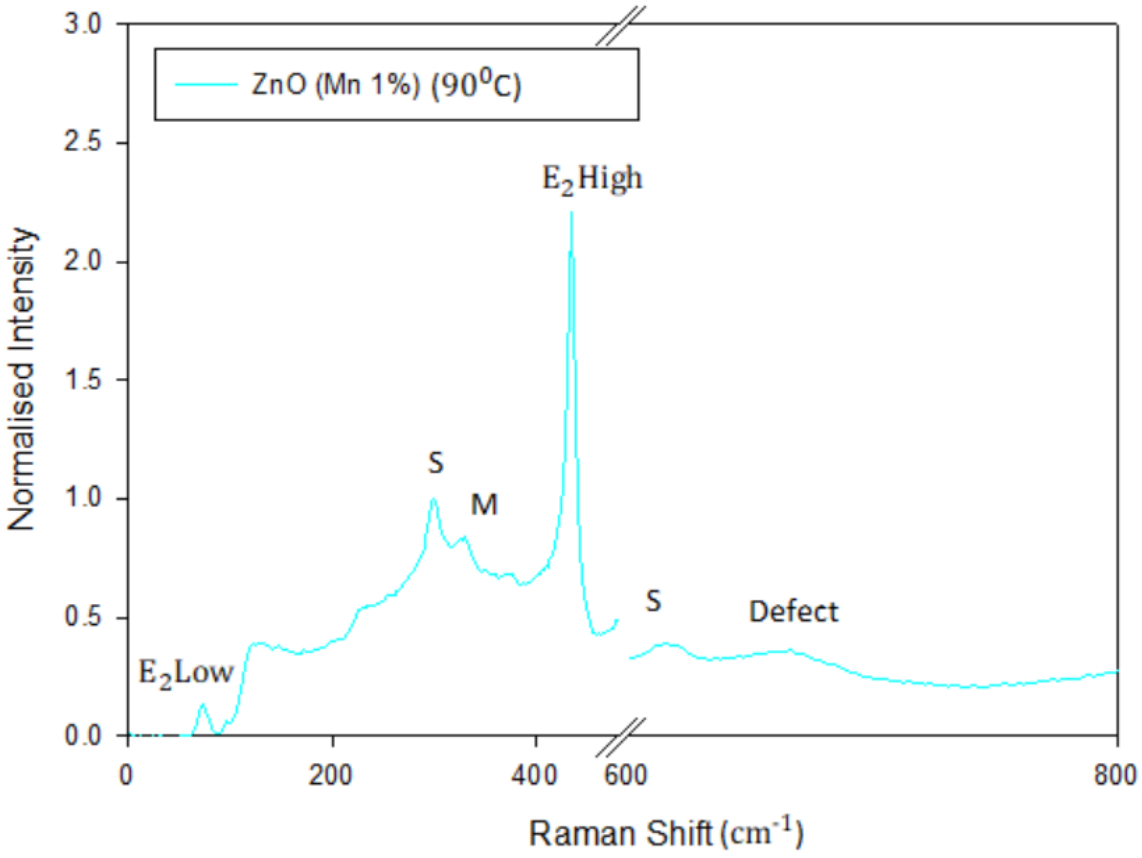


Figure 32: Micro-Raman spectra of ZnO nanorods grown at $90^0$C

Figure 32 shows the $E_2$(H) peak is much sharper than that for samples growth at $70^0$C and $80^0$C as well as lower $E_2$(L) which means that the crystal orientation improved further at $90^0$C. The

sharp $E_2$(H) is evidence of strong wurtzite crystal orientation. Because of the non-flat surface of nanorods there is a M peak in the spectra.

Table 6: Experimental results of the active modes of Mn-doped ZnO nanorods grown at different temperatures

| **Sample** | **$E_2$(H) Peak($cm^{-1}$)** | **$E_2$(L) Peak ($cm^{-1}$)** | **Defects (Peak)($cm^{-1}$)** | **Amplitude of defect peak** |
|---|---|---|---|---|
| ZnO (Mn 1%) $60^0$C | 425.57 | 71.40 | 664.85 | 0.30 |
| ZnO (Mn 1%) $70^0$C | 434.62 | 74.03 | 664.68 | 0.36 |
| ZnO (Mn 1%) $80^0$C | 434.91 | 73.77 | 665.56 | 0.28 |
| ZnO (Mn 1%) $90^0$C | 434.34 | 73.13 | 662.19 | 0.25 |

We can see from the table that when the growth temperature increases from $60^0$C to $70^0$C the defect peak, which is around 663($cm^{-1}$), increases in amplitude. When the temperature increases

to $80^0$C and $90^0$C the amplitude of defect peak decreases, which means higher temperature samples have less defects than those grown at lower temperatures.

## 4.4. Photoluminescence Spectroscopy

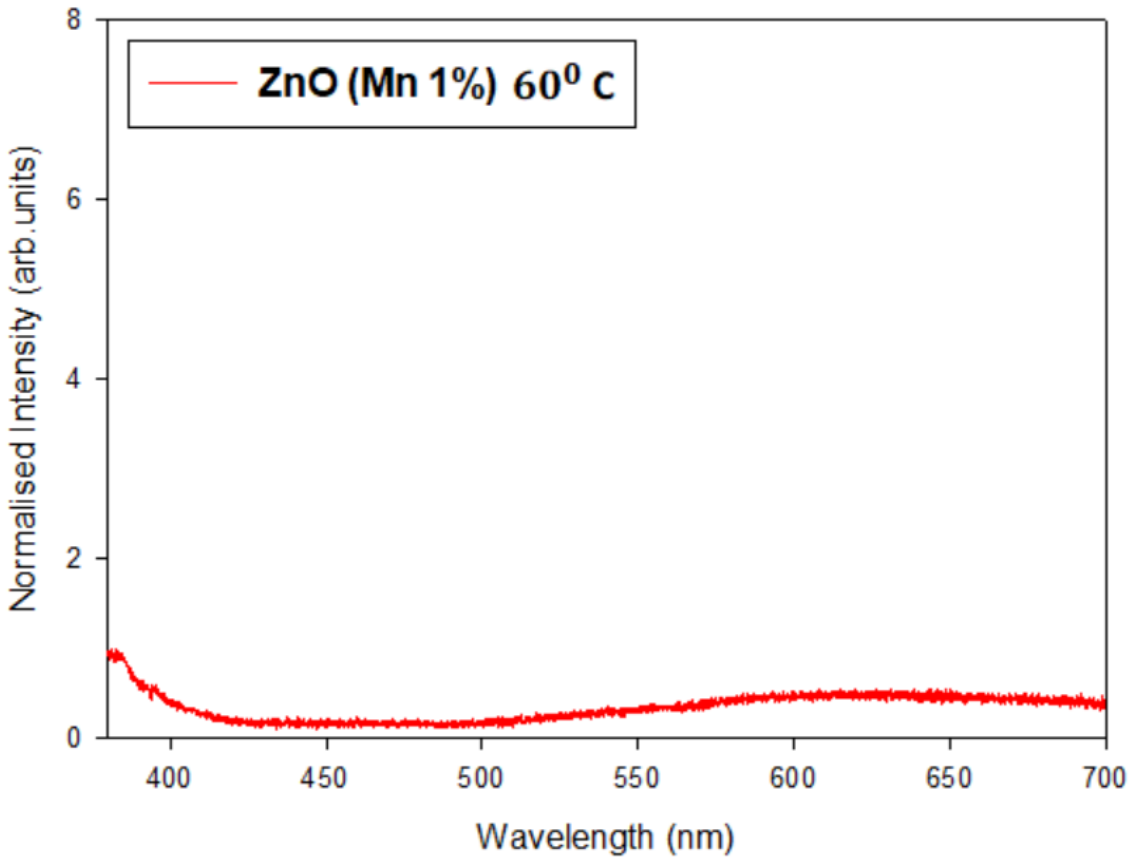


Figure 33: Room temperature photoluminescence of the Mn-doped ZnO nanorods grown at $60^0$C on silicon substrate

In figure 33 we can see the PL spectra of Mn-doped ZnO nanorods grown at $60^0$C temperature. The near band edge (NBE) emission, a narrow peak at 384 nm, was observed. The NBE emission is mainly attributed to free exciton recombination in the ZnO lattice. There is a broad peak around 570 nm to 700 nm that is known as the defect peak. The defect emission peak consists of green, yellow and red emission which originates from different types of defects centers. Defects could be oxygen vacancies, ZnO interstitials, this emission is not strong for samples grown at this low temperature

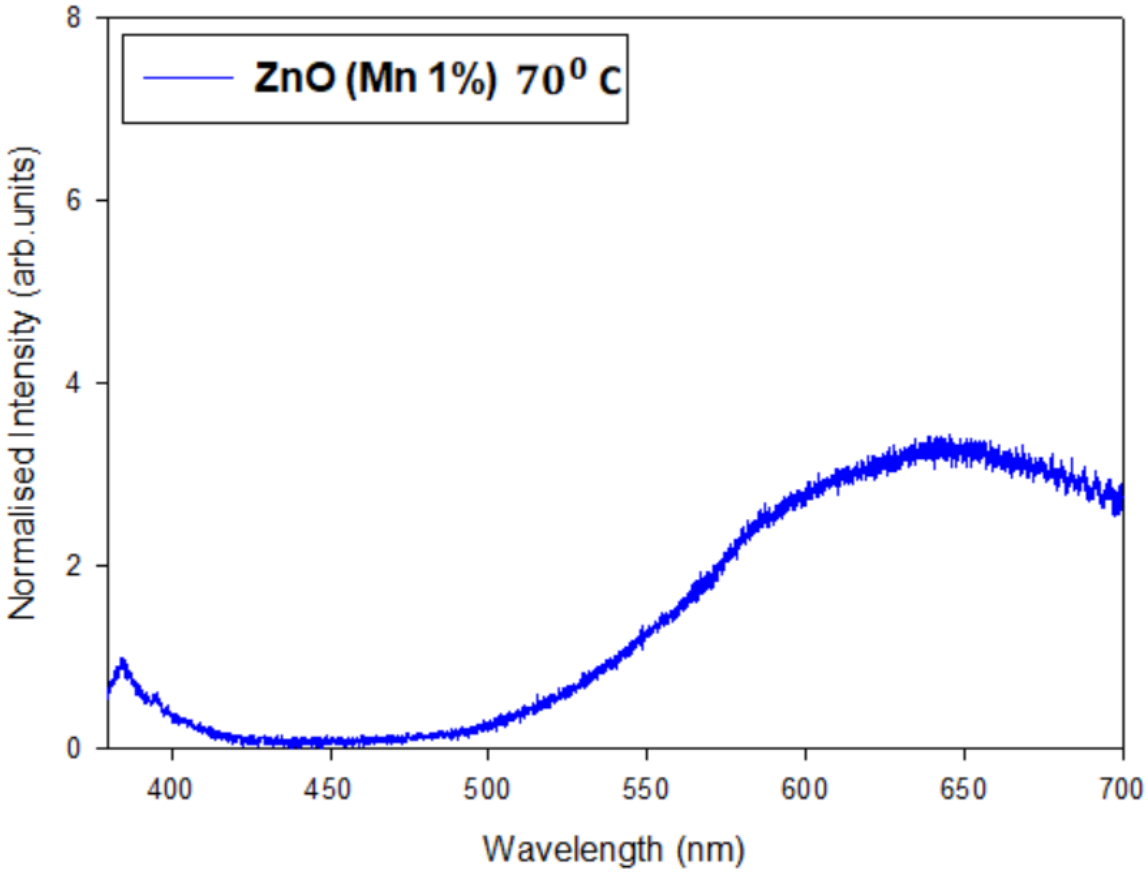


Figure 34: Room temperature photoluminescence of the Mn-doped ZnO nanorods grown at $70^0$C on silicon substrate

The room temperature photoluminescence spectra of Mn- doped ZnO nanorods grown at $70^0$C can be seen in fig.34. We can see that amplitude of defect peak at $70^0$C is increased as compare to $60^0$C. That means that the samples have more defects.

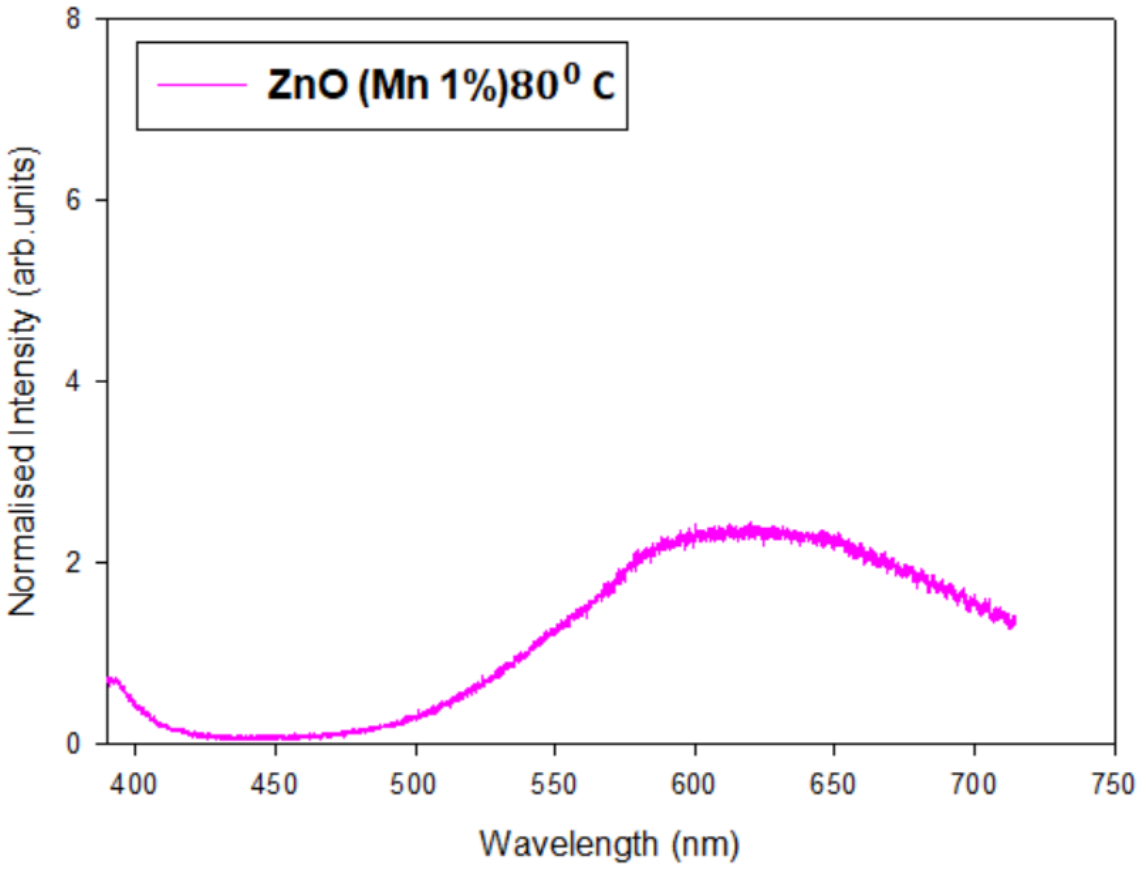


Figure 35: Room temperature photoluminescence of the Mn-doped ZnO nanorods grown at $80^0$C on silicon substrate

The spectra of Mn- doped ZnO nanorods grown at $80^0$C in figure 35 shows that the amplitude of the defect peak at this temperature is smaller than the amplitude of defect emission peak at $70^0$C.

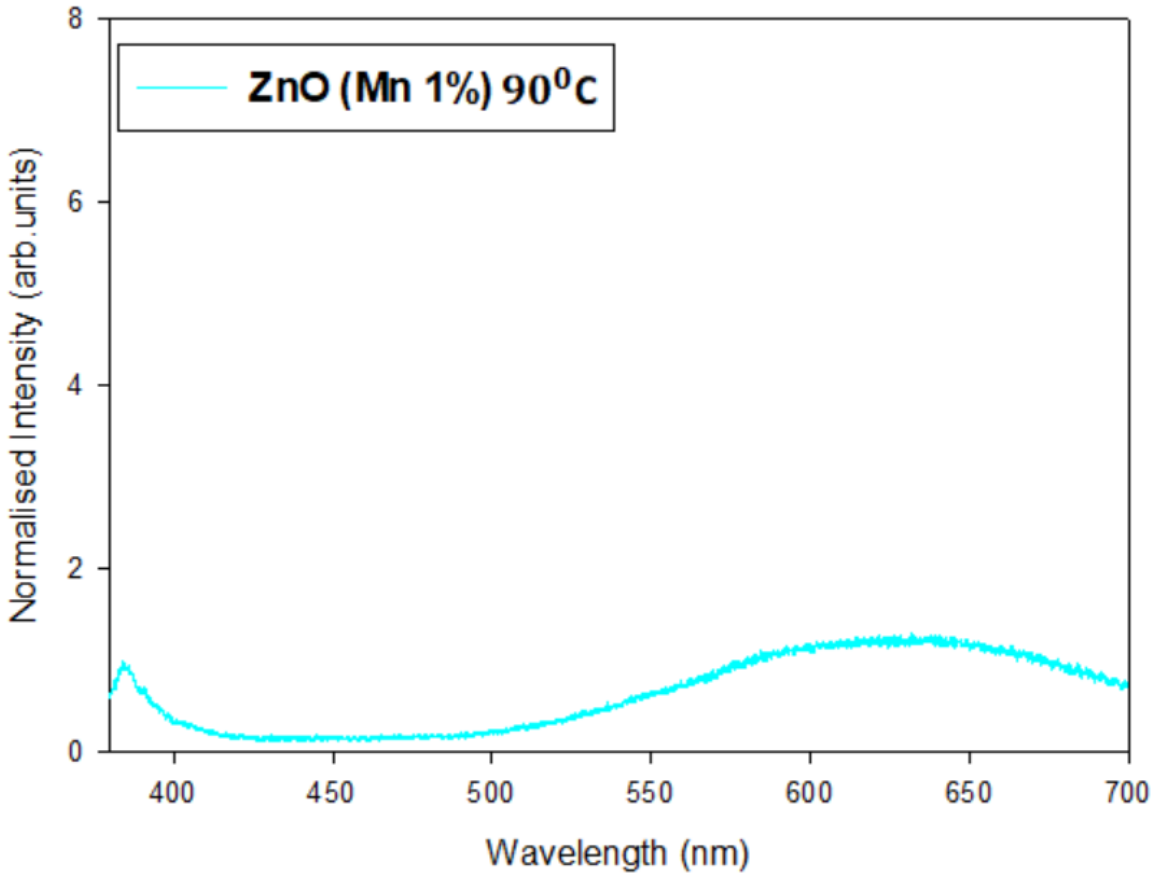


Figure 36: Room temperature photoluminescence of the Mn-doped ZnO nanorods grown at $90^0$C on silicon substrate

Figure 36 shows room temperature Pl spectra of Mn-doped ZnO nanorods grown at $90^0$C, decreased defect emission compared to the $70^0$C temperature samples.

Table 7: Experimental results of the PL spectra of undoped ZnO nanorods grown at different temperatures

| Sample | Defect emission area | Defect emission FWHM | Defect emission peak amplitude |
|---|---|---|---|
| ZnO (Mn 1%) $60^0$C | 114.29 | 221.99 | 0.48 |
| ZnO (Mn 1%) $70^0$C | 631.58 | 315.78 | 3.86 |
| ZnO (Mn 1%) $80^0$C | 489.51 | 301.89 | 3.19 |
| ZnO (Mn 1%) $90^0$C | 302.97 | 279.02 | 1.82 |

We can see from Table that from $60^0$C to $70^0$C, defect emission area, defect emission FWHM, and defect emission peak amplitude increases. After that at $80^0$C and $90^0$C, these factors start decreasing. We can say that at $70^0$C Mn-doped ZnO nanorods have more defects than at other growth temperatures.

# 4.5. ESR Spectroscopy

To get the information about the presence of the transition metal ion in the host ZnO lattice ESR experiments were conducted on these samples.

Since the Mn2+ ions have a similar charge to Zn2+ ions, it is expected that they will be substitutionally located on Zn sites in wurtzite ZnO crystals [51].

The half-filled d shell ($3d^5$) with spin S = 5/2 and angular momentum L = 0 lead to five fine transitions in the ESR spectrum as the H field is changed. The 100% abundant $^{55}$Mn isotope has a nuclear spin I = 5/2. The hyperfine interaction between the $Mn^{2+}$ ion electrons and this nuclear spin leads to 6 hyperfine transitions [52]. The ESR spectrum appearing on $80^0$C and $90^0$C growth temperature Mn-doped ZnO samples arise from the paramagnetic moments of isolated $Mn^{2+}$ ions substitutionally incorporated in the ZnO crystal lattice.

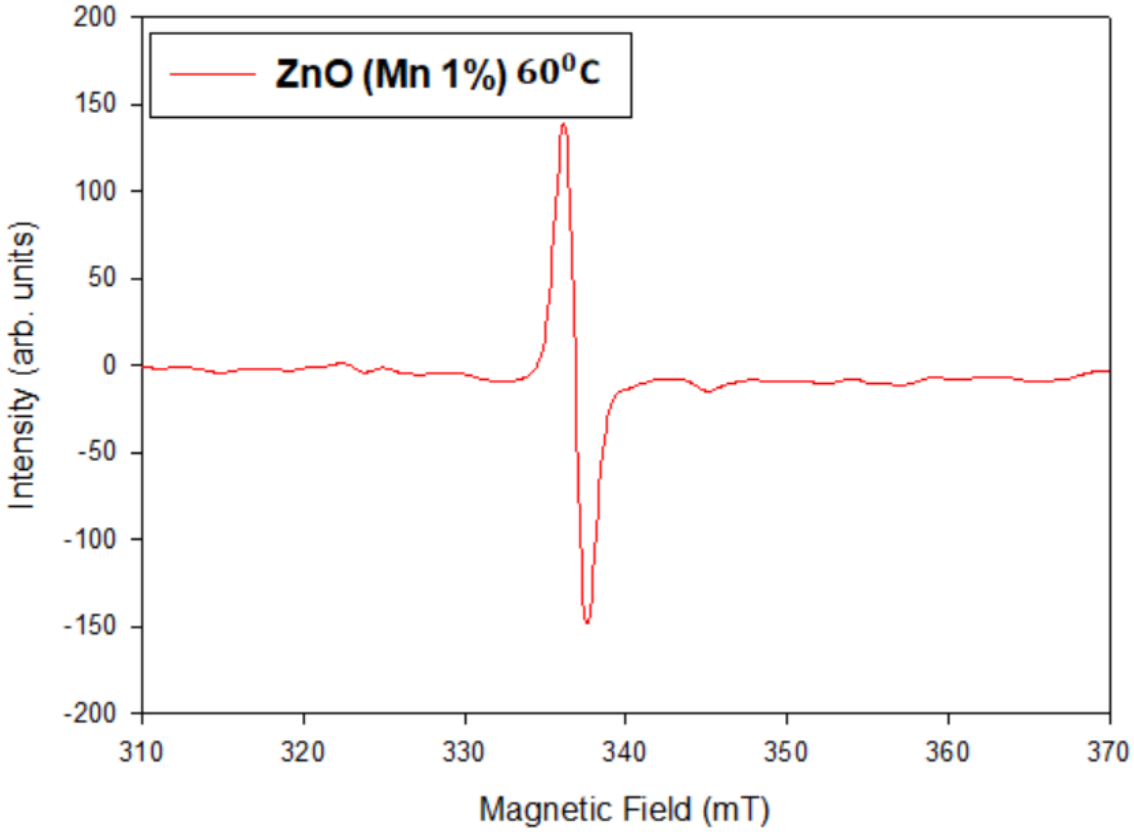


Figure 37: EPR spectrum of Mn-doped ZnO nanorods grown at $60^0$C

For Mn-doped ZnO nanorods grown at $60^0$C, we see a single line signal at g = 1.96 which is attributed to ZnO ESR spectra. There is no signal from $Mn^{2+}$ ions. Which means there was no incorporation of $Mn^{2+}$ions into ZnO nanorods at $60^0$C growth temperature.

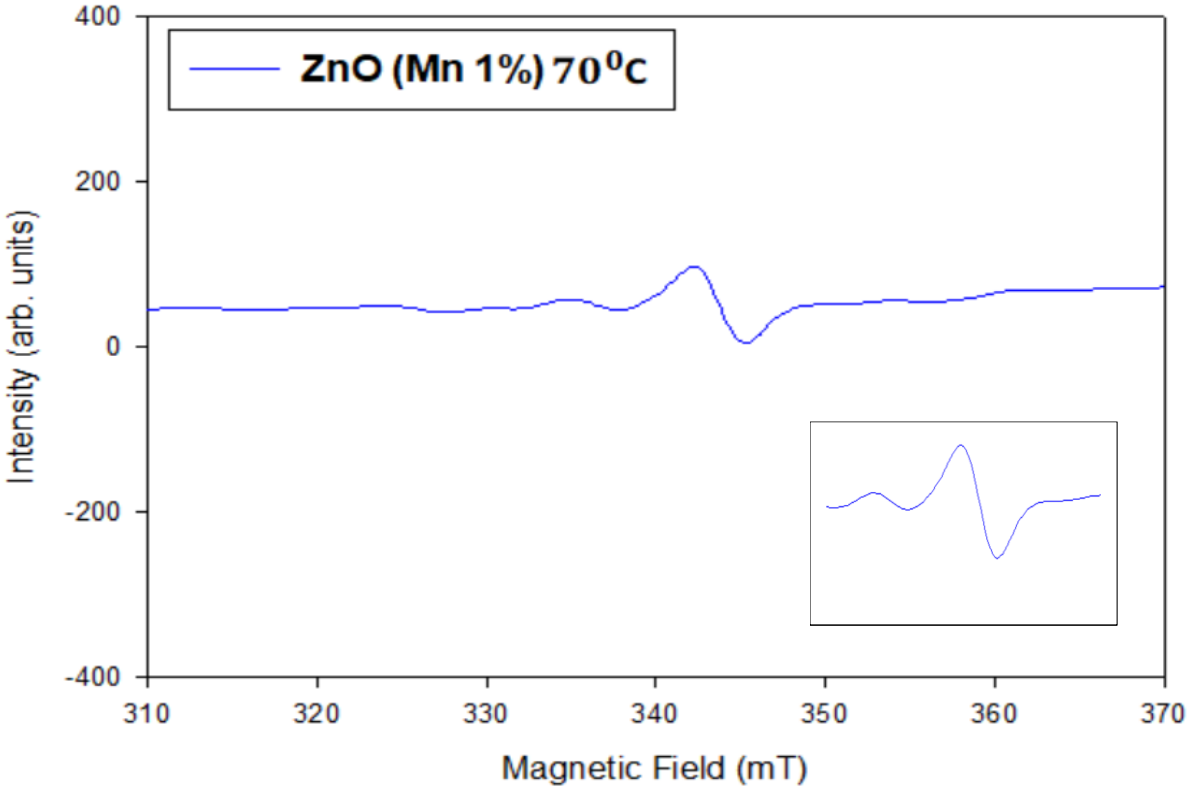


Figure 38: EPR spectrum of Mn-doped ZnO nanorods grown at $70^0$C

From figure 38, we can see that ESR spectra of Mn-doped ZnO nanorods grown at $70^0$C give two-line signals same as undoped ZnO nanorods grown at $70^0$C. which means that at $60^0$C and $70^0$C Mn does not go inside ZnO crystal.

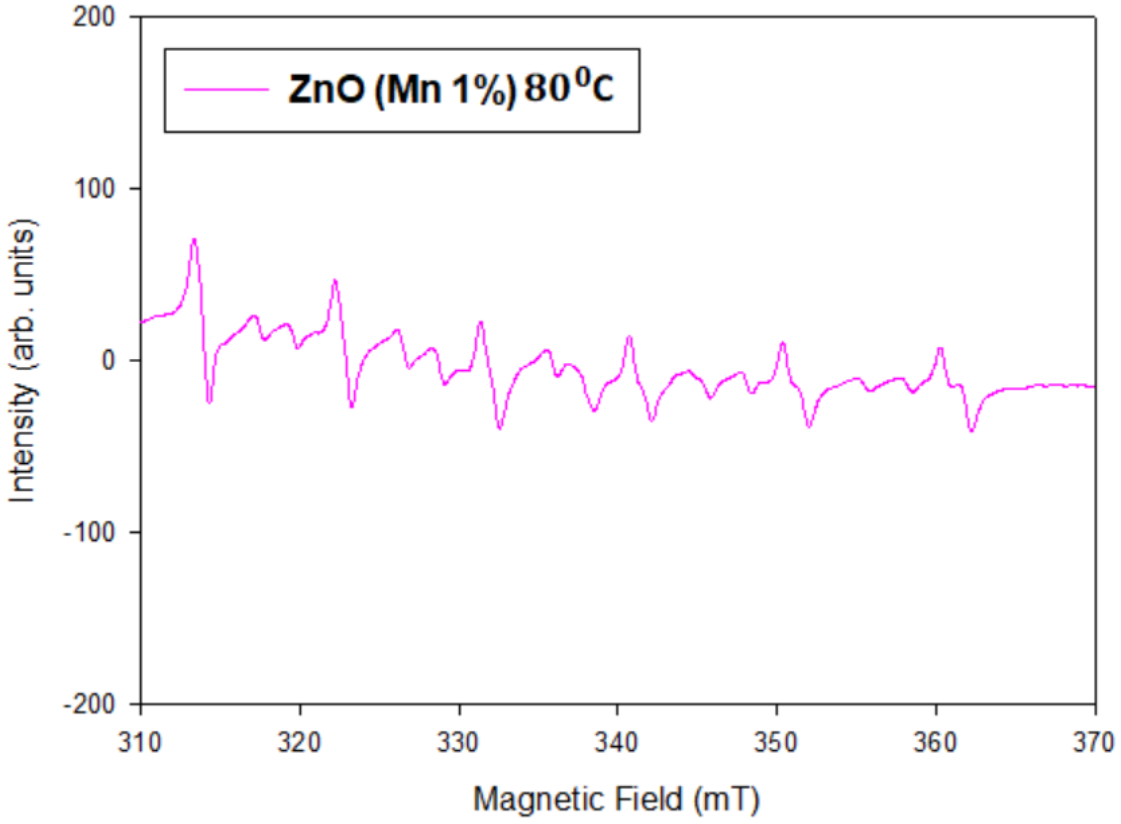


Figure 39: EPR spectrum of Mn-doped ZnO nanorods grown at 80$^0$C

ESR spectra of Mn-doped ZnO nanorods grown at 80$^0$C give multiple line signals. It can be seen from figure 39 that Mn ions incorporate into ZnO. We have multiple ESR lines at this growth temperature. As written before you can see that we have six intense lines and six less intense lines which are related to Mn.

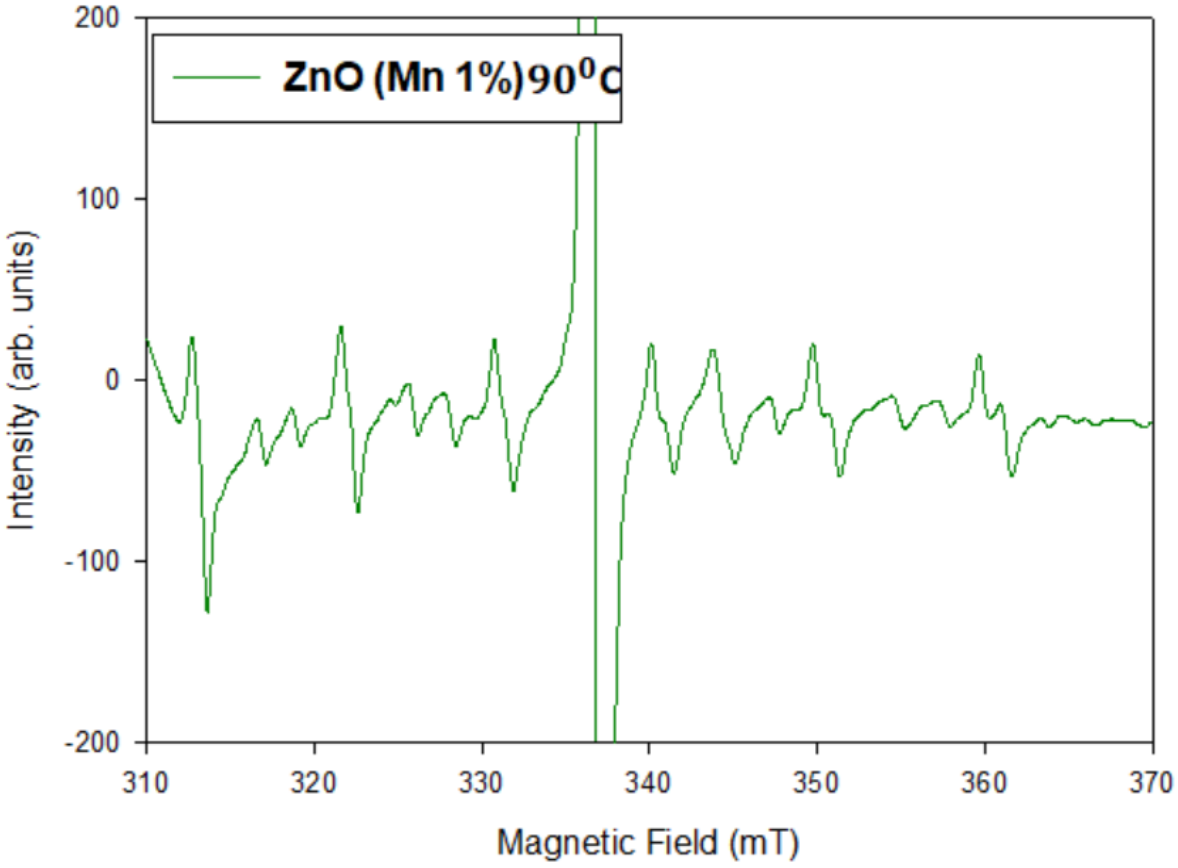


Figure 40: EPR spectrum of Mn-doped ZnO nanorods grown at $90^0$C

It can be seen from figure 40 the ESR spectra of Mn-doped ZnO nanorods grown at $90^0$C, that Mn ions incorporate into ZnO. We have multiple ESR lines for Mn ions at $90^0$C growth temperature. we have six intense lines and six less intense lines which are related to Mn. Also, we do see the spectra for Mn-doped ZnO nanorods samples at $80^0$C and at $90^0$C.

# Chapter 5

# Comparison between undoped and Mn-doped ZnO nanorods

## 5.1. Introduction

In this chapter we will compare the results of our different characterisation techniques for undoped ZnO nanorods and Mn-doped nanorods. We will see the effect of Mn-dopants on the morphology, crystal structure and optical properties.

## 5.2. Morphology

Here we are comparing undoped ZnO nanorods with Mn-doped nanorods at the different growth temperatures.

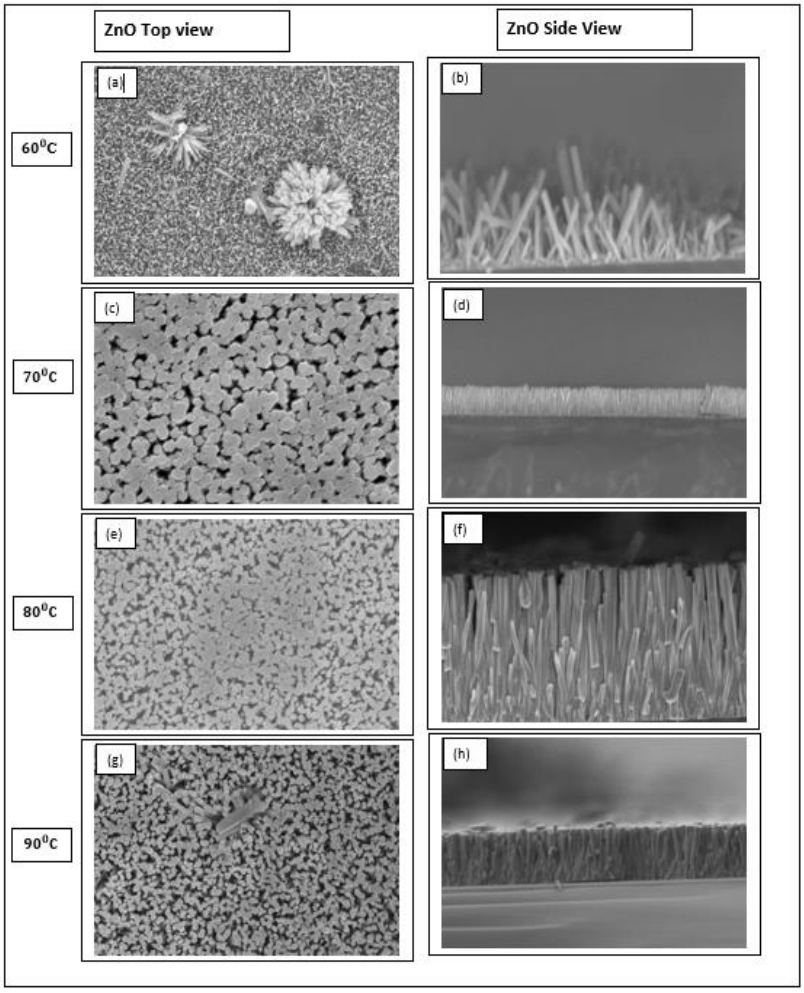


Figure 41: SEM Images of the undoped ZnO nanorods grown at all different temperature

Table 1: Information of size of Undoped ZnO nanorods based on their SEM images

| Sample | Average diameter (nm) | Average length (nm) | Aspect ratio |
|---|---|---|---|
| ZnO 60$^0$C | 68 | 372 | 5.47 |
| ZnO 70$^0$C | 122 | 529 | 4.33 |
| ZnO 80$^0$C | 136 | 1577 | 11.59 |
| ZnO 90$^0$C | 158 | 1620 | 10.25 |

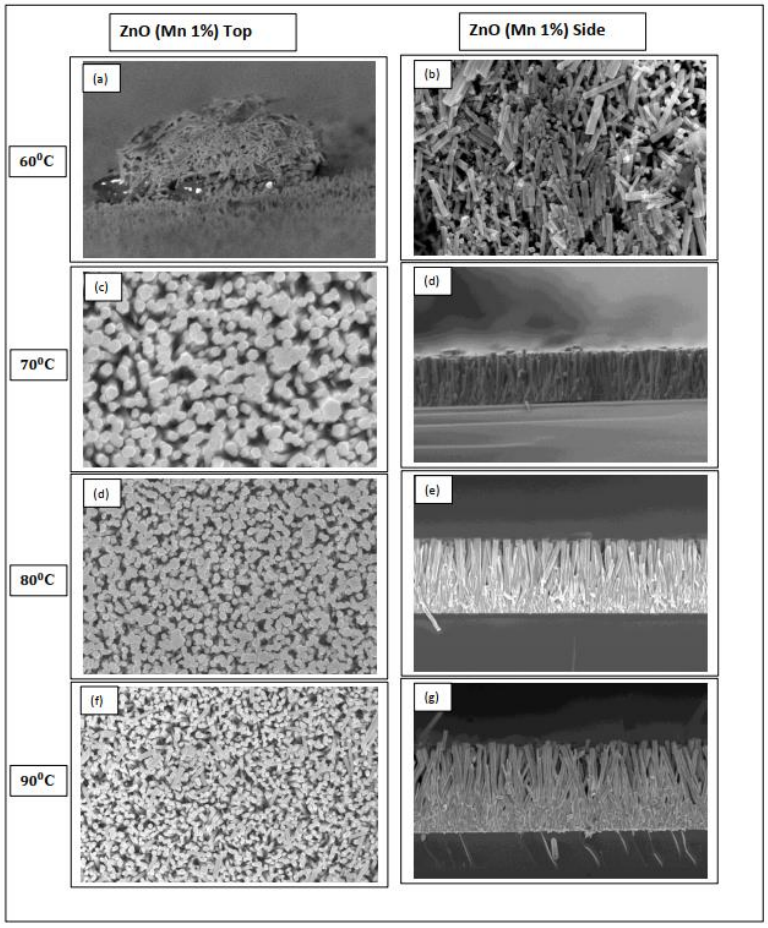


Figure 42: SEM Images of the Mn-doped ZnO nanorods grown at all different temperature

Table 5: Information of size of Mn-doped ZnO nanorods based on their SEM images

| Sample | Average Diameter (nm) | Height (nm) | Aspect ratio |
|---|---|---|---|
| ZnO (Mn 1%) $60^0$C | 69 | 803 | 11.63 |
| ZnO (Mn 1%) $70^0$C | 115 | 861 | 7.48 |
| ZnO (Mn 1%) $80^0$C | 119 | 1622 | 13.63 |
| ZnO (Mn 1%) $90^0$C | 150 | 2782 | 18.54 |

At $60^0$C, the average diameter is comparable between the Mn-doped and undoped nanorods. At $70^0$C, $80^0$C, $90^0$C, the average diameter of the Mn-doped nanorods is slightly smaller. The average length of nanorods is larger for the Mn-doped grown at all temperatures. This generally leads to a better-quality material. In all cases, the aspect ratio of the nanorods is higher for the Mn-doped ones. From this we can deduce that the presence of Mn during the growth results in an enhancement of the vertical growth rate as compared to the lateral one.

# 5.3. Raman Spectroscopy

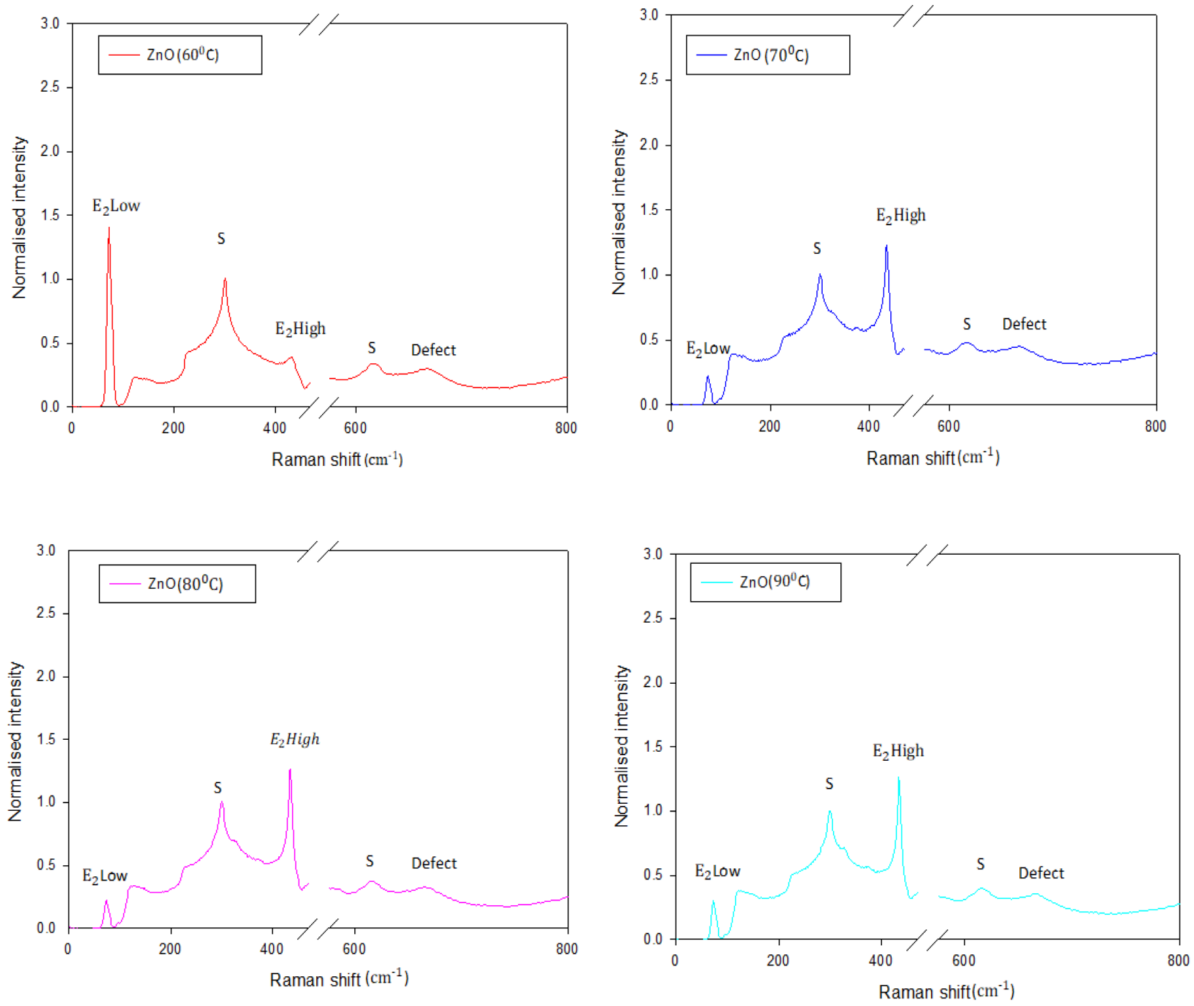


Figure 43: Room temperature Raman Spectra of the undoped ZnO nanorods grown at different temperatures

Table 2: Experimental results of the active modes of undoped ZnO nanorods grown at different temperatures

| Sample | $E_2$(H) Peak($cm^{-1}$) | $E_2$(L) Peak ($cm^{-1}$) | Defects (Peak)($cm^{-1}$) | Amplitude of defect peak |
|---|---|---|---|---|
| ZnO 60$^0$C | 431.52 | 72.29 | 651.06 | 0.32 |
| ZnO 70$^0$C | 434.62 | 74.03 | 658.55 | 0.36 |
| ZnO 80$^0$C | 434.91 | 73.77 | 663.46 | 0.29 |
| ZnO 90$^0$C | 434.34 | 73.13 | 663.12 | 0.22 |

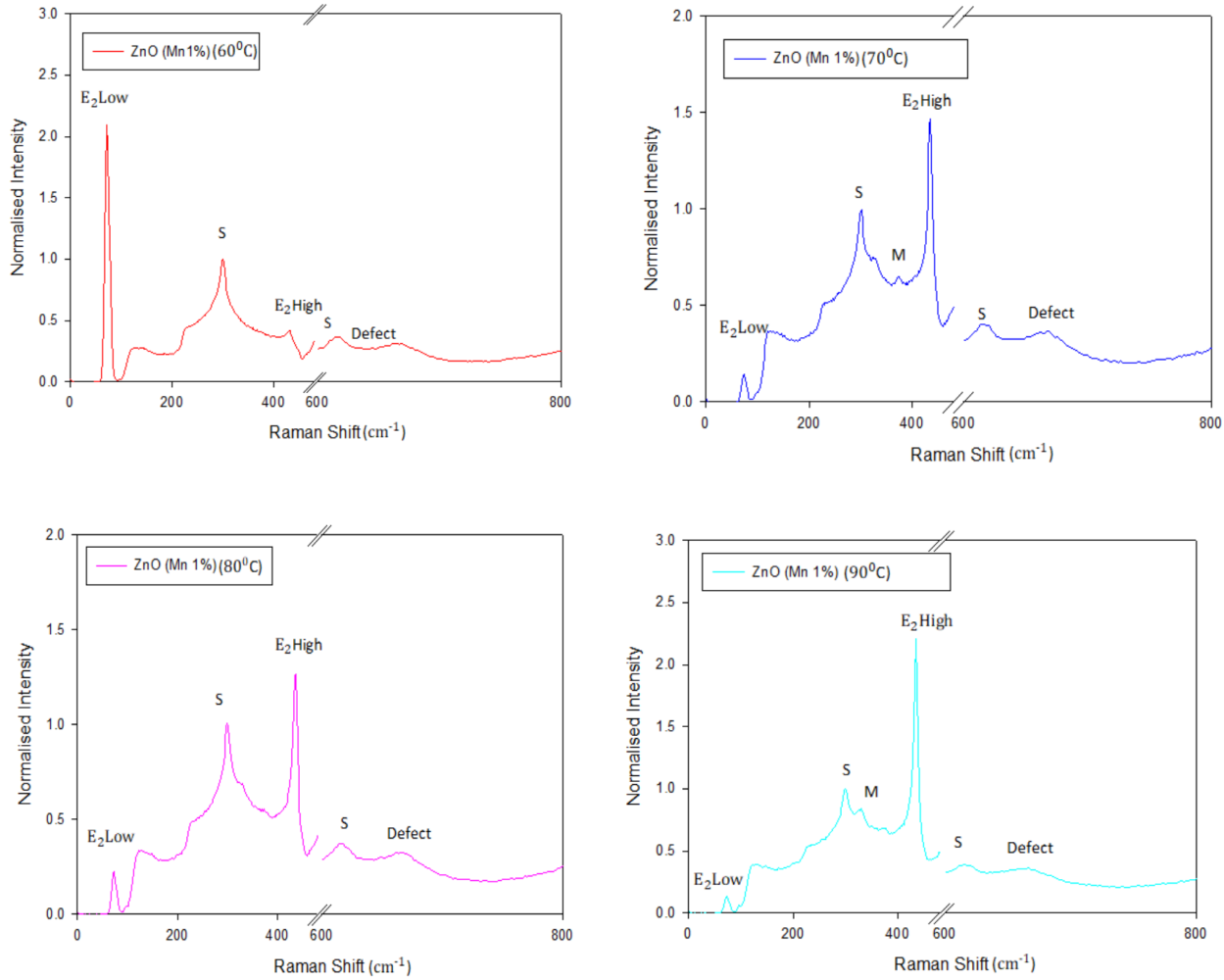


Figure 44: Room temperature Raman Spectra of the Mn-doped ZnO nanorods grown at different temperatures

Table 6: Experimental results of the active modes of undoped ZnO nanorods grown at different temperatures

| **Sample** | **$E_2$(H) Peak($cm^{-1}$)** | **$E_2$(L) Peak ($cm^{-1}$)** | **Defects (Peak)($cm^{-1}$)** | **Amplitude of defect peak** |
|---|---|---|---|---|
| ZnO (Mn 1%) $60^0$C | 425.57 | 71.40 | 664.85 | 0.30 |
| ZnO (Mn 1%) $70^0$C | 434.62 | 74.03 | 664.68 | 0.36 |
| ZnO (Mn 1%) $80^0$C | 434.91 | 73.77 | 665.56 | 0.28 |
| ZnO (Mn 1%) $90^0$C | 434.34 | 73.13 | 662.19 | 0.25 |

If we compare the amplitude of defect peak of ZnO nanorods with Mn doped Zno nanorods, it can be clearly seen from the tables that at $60^0$C, it decreases with Mn-dopant and at $70^0$C there is no change in the amplitudes. At $80^0$C, the amplitude of defect peak decreases and $90^0$C it increases. We can say that at $90^0$C Mn-doped ZnO nanorods has more defects.

# 5.4. Photoluminescence Spectroscopy

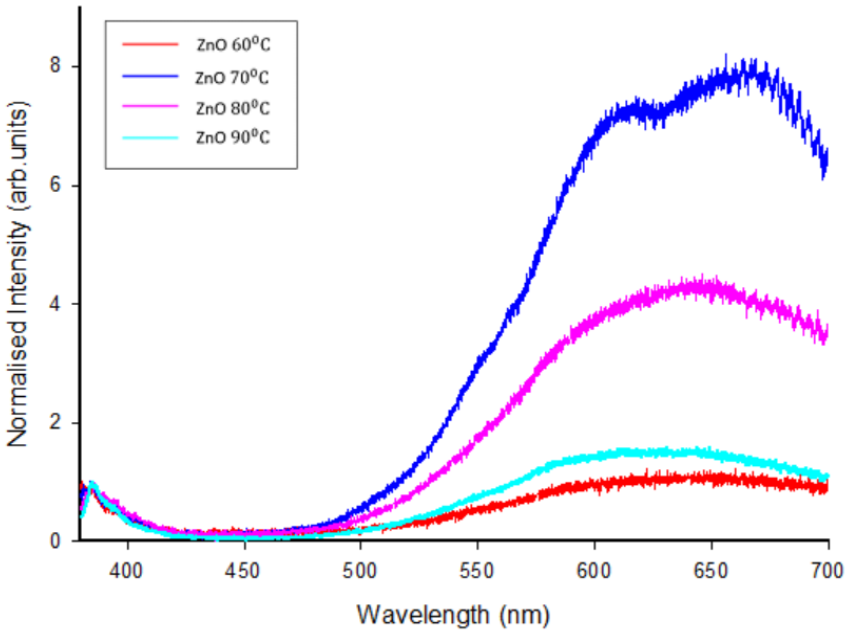


Figure 45: Room temperature PL Spectra of the undoped ZnO nanorods grown at different temperatures

Table 3: Experimental results of the PL spectra of undoped ZnO nanorods grown at different temperatures

| Sample | Defect emission area | Defect emission FWHM | Defect emission peak amplitude |
|---|---|---|---|
| ZnO 60$^0$C | 221.68 | 191.37 | 1.08 |
| ZnO 70$^0$C | 1331.17 | 313.53 | 7.34 |
| ZnO 80$^0$C | 827.23 | 259.82 | 4.97 |
| ZnO 90$^0$C | 284.62 | 236.28 | 1.73 |

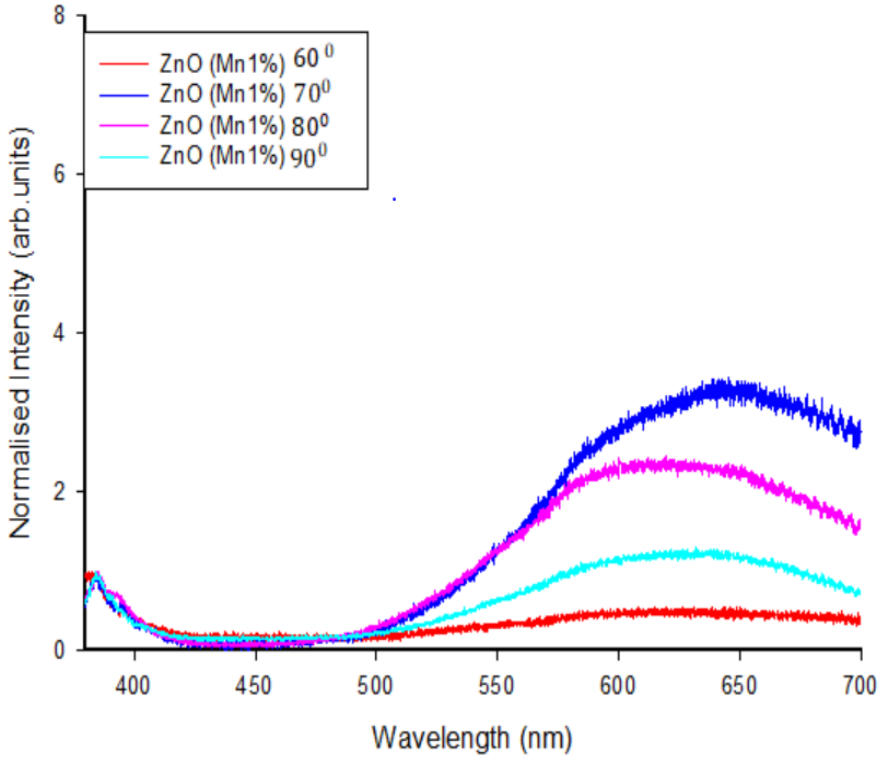


Figure 46: Room temperature PL Spectra of the Mn-doped ZnO nanorods grown at different temperatures

Table 7: Experimental results of the PL spectra of Mn-doped ZnO nanorods grown at different temperatures

| **Sample** | **Defect emission area** | **Defect emission FWHM** | **Defect emission peak amplitude** |
|---|---|---|---|
| ZnO (Mn 1%) $60^0$C | 114.29 | 221.99 | 0.48 |
| ZnO (Mn 1%) $70^0$C | 631.58 | 315.78 | 3.86 |
| ZnO (Mn 1%) $80^0$C | 489.51 | 301.89 | 3.19 |
| ZnO (Mn 1%) $90^0$C | 302.97 | 279.02 | 1.82 |

If we compare the amplitude of defect peak of ZnO nanorods with Mn doped ZnO nanorods, it can be clearly seen from the tables that at $60^0$C, $70^0$C, $80^0$C the amplitude of defect peak decreases with Mn-dopant. At $90^0$C it increases. We can say that at $90^0$C Mn-doped the ZnO nanorods have more defects. We can get less defects in the nanorods at $60^0$C, $70^0$C, $80^0$C. which is consistent with Raman spectroscopy results. Even though the nanorods grown at different temperatures have different lengths, there should be no differences in the PL due to sample cross-section difference. The excitation volume is the same for all samples, given by the excitation microscope objective, and it is at the surface of the nanorod film, so the thickness of the nanorods is not expected not have a major effect. In addition, the normalization procedure using the near band edge emission should eliminate any remaining differences (such as fluctuations in the excitation power).

# 5.5. ESR Spectroscopy

Table 4: Experimental results of ESR spectra of ZnO nanorods at different temperatures ($60^0$C, $70^0$C, $80^0$C, $90^0$C)

| Sample | Line width (core defects) | g-factor | Line width (surface defects) | g-factor |
|---|---|---|---|---|
| ZnO $60^0$C | 1.58 | 1.96 | No line | |
| ZnO $70^0$C | 4.02 | 1.96 | 1.89 | 2.00 |
| ZnO $80^0$C | 1.40 | 1.96 | 1.7 | 2.00 |
| ZnO $90^0$C | 0.58 | 1.96 | 0.93 | 2.00 |

By comparing undoped ZnO nanorods with Mn-doped ZnO nanorods we can see from the ESR spectra that for undoped samples we have core defects at $60^0$C and both core and surface defects at $70^0$C, $80^0$C and $90^0$C.

For Mn-doped ZnO nanorods at $80^0$C and $90^0$C, Mn incorporates into the ZnO crystal. We saw multiple lines signal for samples grown at $80^0$C and $90^0$C. The room temperature ESR spectra at $60^0$C and $70^0$C does not show spectra for Mn-dopant. It just shows the spectra for undoped ZnO nanorods. The most likely reason is that Mn was not incorporated into the ZnO crystal at those growth temperatures.

# Chapter 6

# Conclusions and future approach

We have grown undoped and Mn-doped ZnO nanorods at different temperatures ($60^0$C, $70^0$C, $80^0$C and $90^0$C) on a silicon substrate, using a thin textured film of ZnO nanoparticles known as a seed layer, to compensate for crystal mismatch. These nanorods were synthesised by a hydrothermal method. Overall, our work is one of few works including ESR systematic investigation of growth temperature, and a direct comparison between undoped and $Mn^{2+}$ doped nanorods.

In order to achieve the best crystal orientation, the seed layer must be annealed at temperature of $400^0$C. Raman scattering spectra confirm that as grown nanorods have the wurtzite crystal structure and vertical orientation. Micro PL of undoped and Mn-doped ZnO nanorods shows near band edge emission and a defect emission peak.

The effect of doping and variable growth temperatures on the morphology of the ZnO nanorods was measured by taking the cross-section and top SEM images. Geometry information of the

samples confirms that the variable temperatures and Mn-doping can change the height and diameter of ZnO nanorods.

The optical Raman active modes of undoped and Mn-doped nanorods were measured with a micro-Raman set up at room temperature. A strong $E_2$(H) peak confirms the crystallinity of nanorods. The defect peak which is around 663($cm^{-1}$) gives information about the defects of the nanorods.

Defect emission of undoped and Mn-doped nanorods has been measured by the PL setup at room temperature. A narrow peak at 384 nm was observed, known as near band edge (NBE) emission. NBE emission is mainly attributed to free exciton recombination in the ZnO lattice. There is a broad peak around 570 nm to 700 nm that is known as defect peak. The defect emission peak consists of green, yellow and red emission from the ZnO nanorods which originates from different types of defects centers. Defects could be oxygen vacancies, or ZnO interstitials. We have used the normalised intensity of NBE emission peak in all the PL spectrum. We can see from Table 3 that from $60^0$C to $70^0$C, defect emission area, defect emission FWHM, defect emission peak amplitude increases. After that at $80^0$C and $90^0$C, these factors start decreasing. We can say that at $70^0$C, undoped and Mn-doped ZnO nanorods have more defects.

To see the incorporation of Mn into the ZnO nanorods we have used ESR spectroscopy at room temperature. From ESR spectra we see that for undoped samples we have core defects at $60^0$C and both core and surface defects at $70^0$C, $80^0$C and $90^0$C.

For Mn-doped ZnO nanorods at $80^0$C and $90^0$C, Mn incorporates into the ZnO crystal. We saw multiple lines signal for samples grown at $80^0$C and $90^0$C. The room temperature ESR spectra at $60^0$C and $70^0$C does not show spectra for Mn-dopant. It just shows the spectra for undoped ZnO nanorods which shows that at these temperatures Mn does not incorporate into the ZnO crystal.

From the differences in growth results at different temperatures and with/without dopant, we can infer some insights on the growth mechanism. For instance, when growing nanorods with the Mn precursor in the growth medium leads to wider and taller nanorods at all the tested growth temperatures, even if no presence of Mn can be detected in the ESR characterization. This strongly suggests that the presence of Mn in the growth medium increases the growth rate, both vertical and lateral. This would be the main effect of Mn in the morphology of the nanorods, irrespective of its incorporation in the crystal material, and the most novel finding in this thesis.

From the different characterization of the amount of defects in the material we can also see that their appearance in the crystal structure of the nanorods depends on a complicated way between the temperature and presence of Mn. While the presence of a "bitter spot" at 70 C where the amount of defects found in the crystal is maximal is notorious, more work is needed to determine how this is related to the growth mechanism.

# References


1. Vayssieres, L., Keis, K., Lindquist, S. E., & Hagfeldt, A. (2001). Purpose-built anisotropic metal oxide material: 3D highly oriented microrod array of ZnO. The Journal of Physical Chemistry B, 105(17), 3350-3352.
2. Shrama, S. K., Saurakhiya, N., Barthwal, S., Kumar, R., & Sharma, A. (2014). Tuning of structural, optical, and magnetic properties of ultrathin and thin ZnO nanowire arrays for nano device applications. Nanoscale research letters, 9(1), 1-17.
3. Ahmed, F., Arshi, N., Anwar, M. S., Danish, R., & Koo, B. H. (2013). Mn-doped ZnO nanorod gas sensor for oxygen detection. Current Applied Physics, 13, S64-S68.
4. Yu, C. L., Kim, H., de Leon, N., Frank, I. W., Robinson, J. T., McCutcheon, M., ... & Park, H. (2013). Stretchable photonic crystal cavity with wide frequency tunability. Nano letters, 13(1), 248-252.
5. Könenkamp, R., Word, R. C., & Schlegel, C. (2004). Vertical nanowire light-emitting diode. Applied Physics Letters, 85(24), 6004-6006.
6. Soci, C., Zhang, A., Xiang, B., Dayeh, S. A., Aplin, D. P. R., Park, J., ... & Wang, D. (2007). ZnO nanowire UV photodetectors with high internal gain. Nano letters, 7(4), 1003-1009.

7. Özgür, Ü., Alivov, Y. I., Liu, C., Teke, A., Reshchikov, M., Doğan, S., ... & Morkoç, A. H. (2005). A comprehensive review of ZnO materials and devices. Journal of applied physics, 98(4), 11.

8. Coleman, V. A., Bradby, J. E., Jagadish, C., Munroe, P., Heo, Y. W., Pearton, S. J., ... & Yano, M. (2005). Mechanical properties of ZnO epitaxial layers grown on a-and c-axis sapphire. Applied Physics Letters, 86(20), 203105.

9. Xu, S., & Wang, Z. L. (2011). One-dimensional ZnO nanostructures: solution growth and functional properties. Nano Research, 4(11), 1013-1098.

10. Hassanpour, A., Guo, P., Shen, S., & Bianucci, P. (2017). The effect of cation doping on the morphology, optical and structural properties of highly oriented wurtzite ZnO-nanorod arrays grown by a hydrothermal method. Nanotechnology, 28(43), 435707.

11. Zhou, W., & Wang, Z. L. (Eds.). (2007). Scanning microscopy for nanotechnology: techniques and applications. Springer science & business media.

12. Yu, J. L., Lai, Y. F., Wang, Y. Z., Cheng, S. Y., & Chen, Y. H. (2014). Polarized Raman scattering of single ZnO nanorod. Journal of Applied Physics, 115(3), 033505.

13. Morkoç, H., & Özgür, Ü. (2008). Zinc oxide: fundamentals, materials and device technology. John Wiley & Sons.

14. Chien, C. T., Wu, M. C., Chen, C. W., Yang, H. H., Wu, J. J., Su, W. F., ... & Chen, Y. F. (2008). Polarization-dependent confocal Raman microscopy of an individual ZnO nanorod. Applied physics letters, 92(22), 223102.

15. Yang, J. H., Zheng, J. H., Zhai, H. J., & Yang, L. L. (2009). Low temperature hydrothermal growth and optical properties of ZnO nanorods. Crystal Research and Technology: Journal of Experimental and Industrial Crystallography, 44(1), 87-91.

16. Calleja, J. M., & Cardona, M. (1977). Resonant raman scattering in ZnO. Physical Review B, 16(8), 3753.

17. Giri, P. K., Bhattacharyya, S., Singh, D. K., Kesavamoorthy, R., Panigrahi, B. K., & Nair, K. G. M. (2007). Correlation between microstructure and optical properties of ZnO nanoparticles synthesized by ball milling. Journal of Applied Physics, 102(9), 093515.

18. Umar, A., Kim, S. H., Lee, Y. S., Nahm, K. S., & Hahn, Y. B. (2005). Catalyst-free large-quantity synthesis of ZnO nanorods by a vapor–solid growth mechanism: structural and optical properties. Journal of Crystal Growth, 282(1-2), 131-136.

19. Zhang, R., Yin, P. G., Wang, N., & Guo, L. (2009). Photoluminescence and Raman scattering of ZnO nanorods. Solid State Sciences, 11(4), 865-869.

20. Gayen, R. N., Das, S. N., Dalui, S., Bhar, R., & Pal, A. K. (2008). Zinc magnesium oxide nanofibers on glass substrate by solution growth technique. Journal of crystal growth, 310(18), 4073-4080.

21. Tam, K. H., Cheung, C. K., Leung, Y. H., Djurišić, A. B., Ling, C. C., Beling, C. D., ... & Ding, L. (2006). Defects in ZnO nanorods prepared by a hydrothermal method. The Journal of Physical Chemistry B, 110(42), 20865-20871.

22. Duan, J., Wang, H., Wang, H., Zhang, J., Wu, S., & Wang, Y. (2012). Mn-doped ZnO nanotubes: from facile solution synthesis to room temperature ferromagnetism. CrystEngComm, 14(4), 1330-1336.

23. Sharma, M. K., Gayen, R. N., Pal, A. K., Kanjilal, D., & Chatterjee, R. (2011). Room temperature ferromagnetism in Mn-doped zinc oxide nanorods prepared by hybrid wet chemical route. Journal of alloys and compounds, 509(26), 7259-7266.

24. Liu, X., Wu, X., Cao, H., & Chang, R. P. (2004). Growth mechanism and properties of ZnO nanorods synthesized by plasma-enhanced chemical vapor deposition. Journal of Applied Physics, 95(6), 3141-3147.

25. Khranovskyy, V., Tsiaoussis, I., Hultman, L., & Yakimova, R. (2011). Selective homoepitaxial growth and luminescent properties of ZnO nanopillars. Nanotechnology, 22(18), 185603.

26. Zeze, D. A., Joyce, A. M., Anderson, C. A., & Brown, N. M. D. (2002). Control and mass selection of C n H m+ fragments in an inductively coupled pulsed plasma. Applied physics letters, 80(1), 22-24.

27. Heo, Y. W., Varadarajan, V., Kaufman, M., Kim, K., Norton, D. P., Ren, F., & Fleming, P. H. (2002). Site-specific growth of ZnO nanorods using catalysis-driven molecular-beam epitaxy. Applied physics letters, 81(16), 3046-3048.

28. Cao, B. Q., Lorenz, M., Rahm, A., Von Wenckstern, H., Czekalla, C., Lenzner, J., ... & Grundmann, M. (2007). Phosphorus acceptor doped ZnO nanowires prepared by pulsed-laser deposition. Nanotechnology, 18(45), 455707.

29. Kim, S., Jeong, M. C., Oh, B. Y., Lee, W., & Myoung, J. M. (2006). Fabrication of Zn/ZnO nanocables through thermal oxidation of Zn nanowires grown by RF magnetron sputtering. Journal of Crystal Growth, 290(2), 485-489.

30. Elliott, R. J., & Gibson, A. F. (1974). An introduction to solid state physics and its applications. Barnes & Noble.

31. Umar, A., Kim, S. H., Lee, Y. S., Nahm, K. S., & Hahn, Y. B. (2005). Catalyst-free large-quantity synthesis of ZnO nanorods by a vapor–solid growth mechanism: structural and optical properties. Journal of Crystal Growth, 282(1-2), 131-136.

32. Wertz, J. (2012). Electron spin resonance: elementary theory and practical applications. Springer Science & Business Media.

33. Weil, J. A., & Bolton, J. R. (2007). Electron paramagnetic resonance: elementary theory and practical applications. John Wiley & Sons.

34. Morrish, A. H. (1970). Fizyczne podstawy magnetyzmu. Państwowe Wydawnictwo Naukowe.

35. Eaton, G. R., & Eaton, S. S. (1998). Foundations of modern EPR. World Scientific.

36. Aneesh, P. M., Cherian, C. T., Jayaraj, M. K., & Endo, T. (2010). Co2+ doped ZnO nanoflowers grown by hydrothermal method. Journal of the Ceramic Society of Japan, 118(1377), 333-336.

37. Jakes, P., & Erdem, E. (2011). Finite size effects in ZnO nanoparticles: An electron paramagnetic resonance (EPR) analysis. physica status solidi (RRL)–Rapid Research Letters, 5(2), 56-58.

38. Lima, S. A. M., Sigoli, F. A., Jafelicci Jr, M., & Davolos, M. R. (2001). Luminescent properties and lattice defects correlation on zinc oxide. International Journal of Inorganic Materials, 3(7), 749-754.

39. Yu, B., Zhu, C., Gan, F., & Huang, Y. (1998). Electron spin resonance properties of ZnO microcrystallites. Materials Letters, 33(5-6), 247-250.

40. Sancier, K. M. (1972). Temperature dependence of the electron spin resonance spectra of zinc oxide powder. The Journal of Physical Chemistry, 76(18), 2527-2529.

41. Vanheusden, K., Warren, W. L., Seager, C. H., Tallant, D. R., Voigt, J. A., & Gnade, B. E. (1996). Mechanisms behind green photoluminescence in ZnO phosphor powders. Journal of Applied Physics, 79(10), 7983-7990.

42. Galland, D., & Herve, A. (1970). ESR spectra of the zinc vacancy in ZnO. Physics Letters A, 33(1), 1-2.

43. Kakazey, M., Vlasova, M., Dominguez-Patiño, M., Dominguez-Patiño, G., Srećković, T., & Nikolić, N. (2004). Electron paramagnetic resonance in the research of defect formation and thermal processes during grinding of ZnO powders. Science of Sintering, 36(2), 65-72.

44. Mandal, S. K., Das, A. K., Nath, T. K., & Karmakar, D. (2006). Temperature dependence of solubility limits of transition metals (Co, Mn, Fe, and Ni) in ZnO nanoparticles. Applied physics letters, 89(14), 144105.

45. Djerdj, I., Garnweitner, G., Arčon, D., Pregelj, M., Jagličić, Z., & Niederberger, M. (2008). Diluted magnetic semiconductors: Mn/Co-doped ZnO nanorods as case study. Journal of Materials Chemistry, 18(43), 5208-5217.

46. Liu, J. J., Yu, M. H., & Zhou, W. L. (2005). Well-aligned Mn-doped ZnO nanowires synthesized by a chemical vapor deposition method. Applied physics letters, 87(17), 172505.

47. Singh, A. K., Thool, G. S., Bangal, P. R., Madhavendra, S. S., & Singh, S. P. (2014). Low temperature Mn doped ZnO nanorod array: synthesis and its photoluminescence behavior. Industrial & Engineering Chemistry Research, 53(22), 9383-9390.

48. Panigrahy, B., Aslam, M., & Bahadur, D. (2010). Aqueous synthesis of Mn-and Co-doped ZnO nanorods. The Journal of Physical Chemistry C, 114(27), 11758-11763.

49. Yang, M., Guo, Z., Qiu, K., Long, J., Yin, G., Guan, D., ... & Zhou, S. (2010). Synthesis and characterization of Mn-doped ZnO column arrays. Applied surface science, 256(13), 4201-4205.

50. Yuan, M., Fu, W., Yang, H., Yu, Q., Liu, S., Zhao, Q., ... & Luo, B. (2009). Structural and magnetic properties of Mn-doped ZnO nanorod arrays grown via a simple hydrothermal reaction. Materials Letters, 63(18-19), 1574-1576.

51. Counio, G., Esnouf, S., Gacoin, T., & Boilot, J. P. (1996). CdS: Mn nanocrystals in transparent xerogel matrices: synthesis and luminescence properties. The Journal of Physical Chemistry, 100(51), 20021-20026.

52. Babić-Stojić, B., Milivojević, D., Blanuša, J., Spasojević, V., Bibić, N., Simonović, B., & Arandelović, D. (2008). Ferromagnetic properties of the Zn–Mn–O system. Journal of Physics: Condensed Matter, 20(23), 235217.

53. Zhou, H., Hofmann, D. M., Hofstaetter, A., & Meyer, B. K. (2003). Magnetic resonance investigation of Mn 2+ in ZnO nanocrystals. Journal of applied physics, 94(3), 1965-1968.

54. Ridhuan, N. S., Razak, K. A., Lockman, Z., & Aziz, A. A. (2012). Structural and morphology of ZnO nanorods synthesized using ZnO seeded growth hydrothermal method and its properties as UV sensing. PloS one, 7(11).

55. Singh, A. K., Thool, G. S., Bangal, P. R., Madhavendra, S. S., & Singh, S. P. (2014). Low temperature Mn doped ZnO nanorod array: synthesis and its

photoluminescence behavior. Industrial & Engineering Chemistry Research, 53(22), 9383-9390.

56. Ahmed, F., Arshi, N., Anwar, M. S., Danish, R., & Koo, B. H. (2013). Mn-doped ZnO nanorod gas sensor for oxygen detection. Current Applied Physics, 13, S64-S68.

57. Yu, J. L., Lai, Y. F., Wang, Y. Z., Cheng, S. Y., & Chen, Y. H. (2014). Polarized Raman scattering of single ZnO nanorod. Journal of Applied Physics, 115(3), 033505.

58. Gonzalez, C., Galland, D., & Herve, A. (1975). Hyperfine interactions of the F+ centre in ZnO. Phys. Status Solidi B, 72(1), 309-320.

59. Smith, J. M., & Vehse, W. E. (1970). ESR of electron irradiated ZnO confirmation of the F+ center. Physics Letters A, 31(3), 147-148.

60. K. A. Müller and J. Schneider, Phys. Lett. **4**, 288 1963.

61. Kong, Y. C., Yu, D. P., Zhang, B., Fang, W., & Feng, S. Q. (2001). Ultraviolet-emitting ZnO nanowires synthesized by a physical vapor deposition approach. Applied Physics Letters, 78(4), 407-409.

62. Shojaee, N., Ebadzadeh, T., & Aghaei, A. (2010). Effect of concentration and heating conditions on microwave-assisted hydrothermal synthesis of ZnO nanorods. Materials characterization, 61(12), 1418-1423.

63. Espitia, P. J. P., Soares, N. D. F. F., dos Reis Coimbra, J. S., de Andrade, N. J., Cruz, R. S., & Medeiros, E. A. A. (2012). Zinc oxide nanoparticles: synthesis, antimicrobial activity and food packaging applications. Food and bioprocess technology, 5(5), 1447-1464.

64. Tam, K. H., Cheung, C. K., Leung, Y. H., Djurišić, A. B., Ling, C. C., Beling, C. D., ... & Ding, L. (2006). Defects in ZnO nanorods prepared by a hydrothermal method. The Journal of Physical Chemistry B, 110(42), 20865-20871.

65. Varghese, N., Panchakarla, L. S., Hanapi, M., Govindaraj, A., & Rao, C. N. R. (2007). Solvothermal synthesis of nanorods of ZnO, N-doped ZnO and CdO. Materials Research Bulletin, 42(12), 2117-2124.

66. Chang, Z. (2011). "Firecracker-shaped" ZnO/polyimide hybrid nanofibers via electrospinning and hydrothermal process. Chemical Communications, 47(15), 4427-4429.

67. Jabri, S., Souissi, H., Souissi, A., Meftah, A., Sallet, V., Lusson, A., ... & Oueslati, M. (2015). Investigation of the vibrational modes of ZnO grown by MOCVD on different orientation planes. Journal of Raman Spectroscopy, 46(2), 251-255.